Title

Multielectron Redox and Insulator-to-Metal Transition upon Lithium Insertion in the Fast-Charging, Wadsley-Roth Phase PNb

9
O
25

Journal

Chemistry of Materials, 32(11)

ISSN

0897-4756 1520-5002

Authors

Preefer, Molleigh B
Saber, Muna
Wei, Qiulong
et al.

Publication Date

2020-05-13

DOI

10.1021/acs.chemmater.0c00560

Peer reviewed

Multielectron Redox and Insulator-to-metal Transition upon Lithium Insertion in the Fast-Charging, Wadsley-Roth Phase PNb_9O_{25}

Molleigh B. Preefer,[†,‡] Muna Saber,[¶] Qiulong Wei,[§] Nicholas H. Bashian,[‖] Joshua D. Bocarsly,[‡,⊥] William Zhang,[†] Glenn Lee,[§] JoAnna Milam-Guerrero,[‖] Erica S. Howard,[‖] Rebecca C. Vincent,[‡,⊥] Brent C. Melot,[‖] Anton Van der Ven,[*,⊥] Ram Seshadri,[*,‡,⊥,†] and Bruce S. Dunn[*,§]

†*Department of Chemistry and Biochemistry, University of California Santa Barbara, California 93106, United States*

‡*Materials Research Laboratory, University of California Santa Barbara, California 93106, United States*

¶*Department of Chemical Engineering, University of California Santa Barbara, California 93106, United States*

§*Department of Materials Science and Engineering, University of California Los Angeles, California 90095, United States*

‖*Department of Chemistry, University of Southern California Los Angeles, California 90089, United States*

⊥*Materials Department, University of California Santa Barbara, California 93106, United States*

E-mail: avdv@ucsb.edu; seshadri@mrl.ucsb.edu; bdunn@ucla.edu

Abstract

PNb_9O_{25}, a Wadsley-Roth compound whose structure is obtained by appropriate crystallographic shear of the ReO_3 structure, is a high-power electrode material that can reach 85 % of the equilibrium capacity in 30 minutes and 67% in 6 minutes. Here we show that multielectron redox, as observed through X-ray absorption spectroscopy and X-ray photoelectron spectroscopy, and an insulator-to-metal transition upon lithium insertion, as suggested by a number of complementary techniques, contribute to the impressive performance. Chemically tuning the tetrahedral site between phosphorus and vanadium leads to significant changes in the electrochemistry and kinetics of lithium insertion in the structure, pointing to larger implications for the use of crystallographic shear phases as fast-charging electrode materials.

Introduction

The next-generation of Li-ion batteries requires both higher energy density and higher power to overcome the challenges of breaking with fossil fuels, especially when it comes to electric vehicles. Both increased range and faster charging times are critical to the widespread adoption of electric vehicles, which requires designing new electrode materials.[1] Current anode technology relies mostly upon the use of carbon-based materials (such as graphite), which are unsuitable to fast-charging applications for several reasons. Since the average potential of graphite versus lithium is 0.1 V, the anode faces increased unfavorable reactions with the electrolyte,[2,3] as well as significant dendrite formation especially at high current densities.[4–6] While the former impacts long-term performance in the cells, the latter poses a significant safety issue that can lead to runaway heat generation and explosions.[7] Furthermore, volume expansion leads to significant particle fracturing, especially at high rates.[8] Therefore, anodes with higher voltages and small volume expansion are more suitable for high-power applications, with the compromise of reduced energy density.[3]

There has been a wealth of research on hierarchical and nanoscaled anode materials. Nanostructuring provides the most direct approach to reducing diffusion pathways for lithium to insert, therefore allowing higher rate cycling.[9–11] This approach has proven successful in a variety of materials, particularly TiO_2 and $Li_4Ti_5O_{12}$.[12–14] With the example of $Li_4Ti_5O_{12}$, there is almost zero volume change upon lithium insertion, allowing fast lithium insertion and deinsertion without the negative effects of particle fracturing that degrades the electrode material with repeated cycling, as well as an average voltage of 1.5 V, avoiding the aforementioned issues with cycling to low-voltage.[15,16] However, in order to circumvent the low ionic conductivity in the delithiated and lithiated phases, the material must either be nanostructured or prepared with induced porosity to create short Li diffusion path lengths.[13] Despite starting as electronically insulating, the lithiated phase $Li_7Ti_5O_{12}$ is electronically conductive, which allows for cycling of the material without the addition of conductive carbon additives at reasonably high rates.[16,17] This is not the only example of a host electrode material undergoing an insulator-to-metal transition. The canonical intercalation material $LiCoO_2$, popularized by Goodenough and coworkers and later commercialized,[18] undergoes an insulator-to-metal transition,[19,20] which is highly favorable, especially when it comes to fast cycling when the transition metals are required to aquire and release electrons rapidly.

More recently, crystallographic shear phases derived from the ReO_3 structure — also known as Wadsley-Roth phases — have been popularized for their record-breaking rate-capabilities as electrodes in lithium batteries despite electrodes being prepared with particle sizes on the order of microns.[21–23] While few so far have been studied in-depth to understand the origin of their high rate capabilities, it is believed that the regions of edge-sharing octahedra are the key to success, providing delocalized pathways for electrons, and structural rigidity to suppress large changes in the structure upon lithiation.[24,25] In the absence of crystallographic shear, as in the case of ReO_3, the octahedra are allowed to freely rotate upon lithium insertion, which appears to degrade the material upon cy-

cling.[26,27] Additionally, many Wadsley-Roth phases are attractive electrode materials due to their high capacity as compared to conventional materials, arising from more than one Li ion inserted per transition metal. For example, $TiNb_2O_7$, which is now commercialized, is able to accommodate 1.25 Li per transition metal at a rate of C/5,[24] in conjunction with a small unit cell volume expansion of 7 % when Li^+ is inserted, which is then almost entirely reversible.[28] In the same vein, PNb_9O_{25} has previously been reported to have little lattice expansion upon lithium insertion by *operando* diffraction, about 7.5 %, suggesting promise as a high rate electrode material.[29] Additionally, both of these materials have demonstrated high Li diffusion coefficients, with PNb_9O_{25} three orders of magnitude higher than that of $Li_4Ti_5O_{12}$,[30] further alluding to its promise as a high rate electrode material without nanostructuring.

The existence and preparation of such non-stoichiometric transition metal oxides, including bronze phases and Wadsley-Roth phases[31–34] have been known since the 1950s and 1960s. Chemical and electrochemical lithium insertion into these materials began in the 1980s. Seminal work by Murphy *et al.*[35,36] and Cava *et al.*[37] introduced reversible lithiation in shear phases such as V_6O_{13}, $TiNb_2O_7$, Nb_2O_5, $W_8Nb_{18}O_{69}$, $W_{2.5}V_{0.5}O_7$, and VNb_9O_{25}. Through the amount of lithium inserted, and later through *ex situ* and *operando* diffraction, it was presumed that a common trait of these crystallographic shear structures is more than one Li inserted per transition metal.[29,36,38,39]

PNb_9O_{25} is an interesting model system to study in the realm of the Wadsley-Roth crystallographic shear structures, in that most of the structures contain only corner- and edge-sharing octahedra. First reported in 1965 by Roth *et al.*,[31,40] the structure of PNb_9O_{25} is created from shearing 3×3 blocks of ReO_3-type metal-oxygen octahedra, leaving space for a tetrahedral bridging site between blocks (Figure 1), which has been refined to be half-occupied.[41] The phosphorus is incorporated in PO_4 tetrahedra and can also be substituted by redox-active vanadium, and presumably other elements that have affinities for tetrahedral environments, in the same crystal structure. While the small abundance of phosphorus

and vanadium initially seems inconsequential, the difference between a redox active and redox inactive element in the tetrahedral site changes the fundamental redox mechanisms underlying the battery performance. This opens a wide range of chemical tuning to target electrochemical properties of interest in identical structures. Interestingly, incorporating vanadium actually leads to a decrease in rate performance and capacity retention despite providing another redox active element. The comparison between PNb_9O_{25} and VNb_9O_{25} shows that small chemical changes within these structures can lead to disproportionately large electrochemical differences.

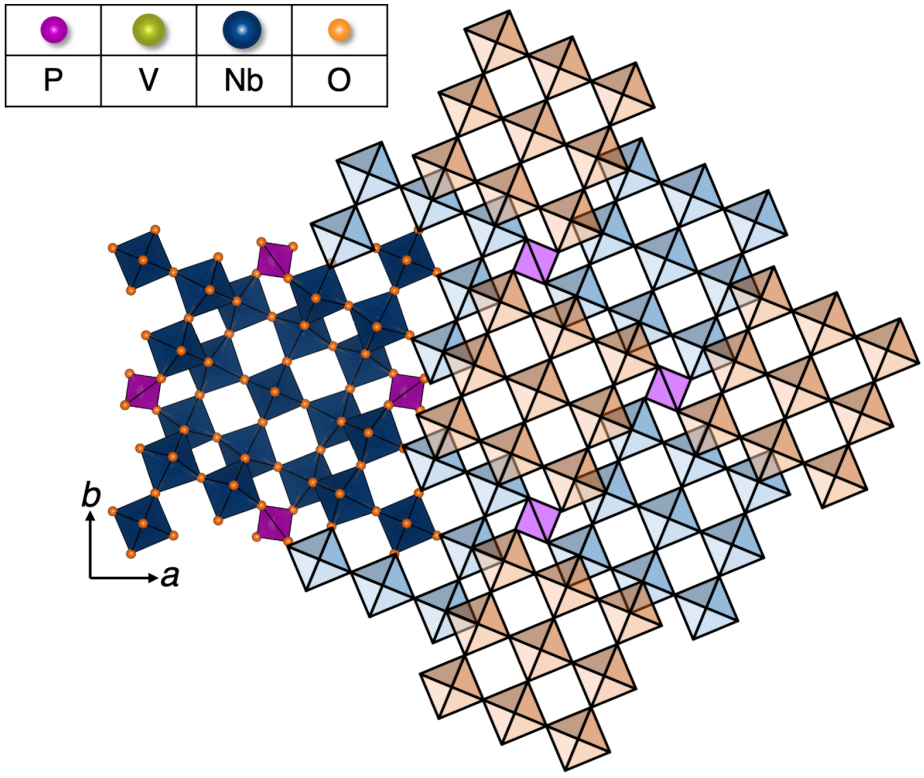

Figure 1: Crystal structure of PNb_9O_{25} as derived from the ReO_3 structure. On the left is the real structure, and on the right, a scheme comprising $3\times3\times1$ blocks of Nb–O octahedra offset to create corner- and edge-sharing moieties. P (or V) bridge the offset Nb–O blocks with half-occupancy on the tetrahedral site. The distinct colors of the octahedral blocks on the right indicate their relative positions along the c direction. The space group is $I4/m$ (# 87).

We report fast, reversible cycling up to 60C in PNb_9O_{25} and VNb_9O_{25} on the order of microns, with greater capacity in PNb_9O_{25} despite having fewer redox active elements, as well

as high capacity retention over 500 cycles at a rate of 2C. This motivates the practical use of PNb_9O_{25} as a next-generation Li-ion electrode material that can be charged to 85% of its theoretical capacity in 30 minutes, even without much electrode optimization. Kinetic analysis shows the underlying difference in rate performance in PNb_9O_{25} and VNb_9O_{25} to be related to many redox reactions in PNb_9O_{25} being surface-controlled versus bulk-controlled in VNb_9O_{25}. Additionally, X-ray absorption near-edge spectroscopy (XANES) and X-ray photoemission spectroscopy (XPS) provide direct evidence of multielectron redox in both materials and point to the fundamental cause for electrochemical differences in these isostructural electrode materials. Finally, through a combined experimental and computational approach, we propose the occurrence of an insulator-to-metal transition in PNb_9O_{25}, which likely is a larger feature of crystallographic shear structures with channels of edge-sharing octahedra, as suggested here from Density Functional Theory-based calculations of the electronic structure of pristine and lithiated PNb_9O_{25}.

Methods

Solid-state preparation of PNb_9O_{25} and VNb_9O_{25}

PNb_9O_{25} and VNb_9O_{25} were prepared using bulk solid state methods, starting from stoichiometric ratios of Nb_2O_5 (Materion, 99.95%) and $(NH_4)_3PO_4$ (Sigma Aldrich, 98%) or Nb_2O_5 (Materion, 99.95%) and V_2O_5 (Materion, 99.9%), respectively, following previous procedures.[29,42] To prepare PNb_9O_{25}, a ground stoichiometric mixture of Nb_2O_5 and $(NH_4)H_3PO_4$ was pressed into a 6 mm pellet under 2.5 metric tons of force with a total mass of 500 mg. Pellets were annealed in an alumina crucible in air at 623 K for 20 h and subsequently annealed at 1523 K for 18 h before being allowed to slow cool. To prepare VNb_9O_{25} a ground stoichiometric mixture of Nb_2O_5 and V_2O_5 was pressed into 6 mm pellets under 2.5 metric tons with a total mass of 500 mg. Pellets were annealed in an alumina crucible in air at 1053 K for 48 h, and then allowed to slow cool. Purity was con-

firmed through powder diffraction data collected at the high-resolution beamline 11-BM at the Advanced Photon Source at Argonne National Laboratory for PNb_9O_{25} ($\lambda = 0.457841$) and at the high-throughput beamline 17-BM for VNb_9O_{25} ($\lambda = 0.4524$ Å). The patterns were refined using the Rietveld method using TOPAS Academic v6. Both patterns were well-refined within previously reported structures in the $I4/m$ (# 87) space group.[41,43]

Electrochemical testing

The active material was cast on copper foil in a ratio of 75% active material, 10% polyvinylidene fluoride (Solef), and 15% carbon black (TIMCAL Super P). First, the active material was ball milled for 30 minutes with the appropriate ratio of carbon black in a 2 cm^3 canister. The active material/carbon mixture was then added to a mixing cup with PVDF dissolved in NMP. The slurry was mixed in a FlackTek speed mixer at 2000 rpm for 15 minutes. Approximately 1.5 cm^3 of NMP was used for 100 mg of slurry. The slurry was cast onto copper foil using a 150 μm doctor blade, dried under vacuum at 90 °C, and punched into 10 mm diameter discs such that there is approximately 1.5 mg cm^{-2}. The cells were cycled in coin cell configuration (MTI parts, 2032 SS casings) using 1 M $LiPF_6$ in EC/DMC 50/50 *v/v* (Sigma Aldrich) versus a polished Li foil counter electrode with Celgard C480 polypropylene/polyethylene separators. Based on the number of pockets for Li to sit and the number of redox-active elements, 12 Li were assumed to insert into PNb_9O_{25}, and 14 Li were assumed to insert into VNb_9O_{25} for calculating C rates, *e.g.* for PNb_9O_{25}: C/10 = $12Q/10$ = 254 mAh g^{-1}/10 h = 25.4 mA g^{-1}; for VNb_9O_{25}: C/10 = $14Q/10$ = 292 mAh g^{-1}/10 h = 29.2 mA g^{-1}. Here Q is the charge.

X-ray photoelectron spectroscopy

The same samples prepared for *ex situ* X-ray diffraction were used for XPS and were loaded onto an air-free sample holder in an Ar-filled glovebox. The powder was spread onto

double-sided scotch tape attached to a stainless steel sample holder. A lid with an o-ring seal was secured onto the sample holder to transfer the samples into the XPS chamber. Once under vacuum, the lid was removed such that the samples were never exposed to air. The samples were measured using a Thermo Fisher Escalab Xi+ XPS equipped with a monochromated Al anode (E = 1486.7 eV). Survey scans were collected at 100 eV pass energy for 20 ms, averaged 2 times. High resolution scans were collected in the Nb 3d, P 2p, V 2p, O 2p, and Li 1s regions at 20 eV pass energy for 100 ms, averaged 15 times. All spectra were referenced to adventitious carbon at 284.8 eV. Fits were executed using CasaXPS: Shirley backgrounds, GL(30) peak shapes, and peaks within elemental regions with spin-orbit splitting were locked to their appropriate ratios and energy splitting according to the element.

Operando X-ray Absorption Spectroscopy

Pellet electrodes were fabricated with 60% active material, 10% acetylene black, 10% graphite powder (300 mesh) and 20% polytetrafluoroethylene (Sigma Aldrich, 1 um average particle size), pressed in a 10 mm die under a hydrostatic pressure of 1 metric ton with approximately 20 mg total material. The pellet electrodes were cycled versus polished Li foil with glass fiber GF/D separators soaked in $LiPF_6$ in EC/DMC 50/50 *v/v* in AMPIX cells at Beamline 12-BM at the Advanced Photon Source, Argonne National Laboratory. This method was adapted from Borkiewicz *et al.*[44] The cells were cycled at a C/10 rate. Simultaneously, the absorption was measured at the Nb K-edge (18.9 keV), calibrated using Nb foil. Data was collected in transmission mode over 8 minutes. Processing and analysis of the XANES region was done using ATHENA, an open source software package for XAS, and the edge position was determined by the zero-crossing of the second derivative.[45]

Magnetic susceptibility measurements

$Li_xPNb_9O_{25}$ at discrete lithiated states was prepared in 1.5 inch diameter Swagelok cells to accommodate approximately 100 mg of pure PNb_9O_{25} powder in a thin layer without the addition of binder or carbon. The active material was cycled against polished Li metal using 1 M $LiPF_6$ in EC/DMC 50/50 *v/v* (Sigma Aldrich). The cells were discharged at a C/60 rate to the chosen potentials. The active material was extracted from the cells in an Ar-filled glovebox and ground with an agate mortar and pestle. Magnetic susceptibility as a function of temperature was collected using a Quantum Design Magnetic Property Measurements System (MPMS-3). Measurements were performed on three powder samples with different levels of lithiations, with no binder or additive. The cells were discharged to 1.75 V, 1.4 V, and 1 V corresponding to $Li_{1.8}PNb_9O_{25}$, $Li_{8.0}PNb_9O_{25}$, and $Li_{11.2}PNb_9O_{25}$, respectively. Weighed, powdered samples were loaded into sealed polypropylene capsules within an argon glovebox and transferred to the magnetometer without exposure to air. From magnetization *vs.* field hysteresis loops at room temperature, all samples were found to contain small amounts of a ferromagnetic impurity, which was traced back to the ball-milling process. In order to measure the true susceptibility of the bulk sample without the ferromagnetic impurity signal, magnetization measurements at each temperature were performed at two different fields which were chosen to be above the field at which the ferromagnetic impurity saturates. The differential magnetic susceptibility was then calculated from those data points. Details of this procedure are provided in the Supporting Information.

Nuclear Magnetic Resonance

Solid-state MAS ^{31}P NMR spectra were acquired on a Bruker AVANCE III Ultrashield Plus 800 MHz (18.8T) NMR spectrometer equipped with a Bruker 2.5mm HX MAS probe. PNb_9O_{25} was packed in a 2.5 mm zirconia rotor in air. $Li_{11.2}PNb_9O_{25}$ was prepared iden-

tically to the sample described for the corresponding EIS measurement (discharged to 1 V) and was packed in a 2.5 mm zirconia rotor in an Ar-filled glovebox. Both spectra were referenced to solid triphenylphosphine and processed using Bruker TopSpin software. The recycle delay was optimized and found to be 3.2s for quantitative analysis. Single pulse experiments were used to obtain the 1d spectra.

Electronic structure calculations

Density functional theory (DFT) calculations were performed with the Vienna *ab initio* Simulation Package (VASP)[46–49] using the Perdew-Burke-Ernzerhof (PBE) functional.[50] The plane wave basis energy cutoff was set at 550 eV. All relaxations were followed with static calculations. The fully relaxed energies of a total of 1130 different Li-vacancy orderings over horizontal and vertical square coordinated sites within the blocks, and square pyramidal sites within the edges of the blocks of the PNb_9O_{25} host were calculated. Benchmark calculations showed that spin polarization has a negligible effect on the energies, and subsequent relaxations were performed in the absence of spin polarization. For each of the calculated ground state configurations, the spin polarized electronic density of states was calculated. A k-point mesh of density 50 Å was employed. Charge density calculations were performed for bands beneath and within the range of the Fermi level. Gaussian smearing was used with a width of 0.1 eV. Visualization of the Nb t_{2_g} state density on discrete lithiated states was done using VESTA.[51]

Results and discussion

Electrochemical properties

Understanding the electrochemistry of PNb_9O_{25} is enhanced by comparing it to its closely related counterpart VNb_9O_{25}. Despite PNb_9O_{25} and VNb_9O_{25} being isostructural, varying

the tetrahedral site atom immensely alters the electrochemistry and mechanism in which lithium inserts into the structure, particularly at varying rates and over long-term cycling. This is especially surprising given the low abundance of phosphorus or vanadium in the structure. The difference, however, lies in the fact that vanadium is redox active, whereas phosphorus is redox inactive, lending a clue into the importance of the surrounding pocket sites or pyramidally coordinated sites available for lithium to insert. PNb_9O_{25} exhibits more structure in its galvanostatic response, which can be observed in detail when cycled slowly at a C/20 rate [Figure 2(a)]. There is a small initial plateau at 1.95 V that incorporates about 0.3 Li experimentally, which leads into a sloped region until about 1.69 V for a total of 1.85 Li. The largest plateau at 1.69 V ends at about 4.5 Li, and then a large, undulating sloping region incorporates up to 10.3 Li total. Finally, there is a small plateau at 1.6 V, and a total of about 11.5 Li inserts into the structure. The capacity loss associated with the first charge is the largest, 1 Li, but thereafter is only small fractions of Li. The structure of the galvanostatic curve maintains its integrity throughout cycling, and the slopes and plateaux are highly repeatable.

The galvanostatic behavior from inserting Li into VNb_9O_{25} shows a quite different profile [Figure 2(b)]. The first discharge has a large sloping region incorporating about 4 Li, a small plateau at 1.7 V inserting a total of 7 Li, and a large sloping region until about 13.5 Li. The subsequent charge is much less reversible – more than 3 Li are not removed. This is in agreement with previous slow cycling results on both micron-sized and nano-sized particles.[29,37,52] Subsequent cycles do not exhibit the same large sloping region at the beginning of discharge. The capacity loss cycle-to-cycle is much more significant than with PNb_9O_{25}. For both materials, the lower voltage cutoff (1 V) was chosen to avoid convolution with Li storage in carbon, which can add anomalous capacity.[53]

When the rate is increased to 2C, the differences in electrochemistry are further exacerbated [Figure 2(c) and (d)]. The same plateau and structure are maintained in the PNb_9O_{25} electrochemical curve, with slightly increased polarization. VNb_9O_{25} still exhibits

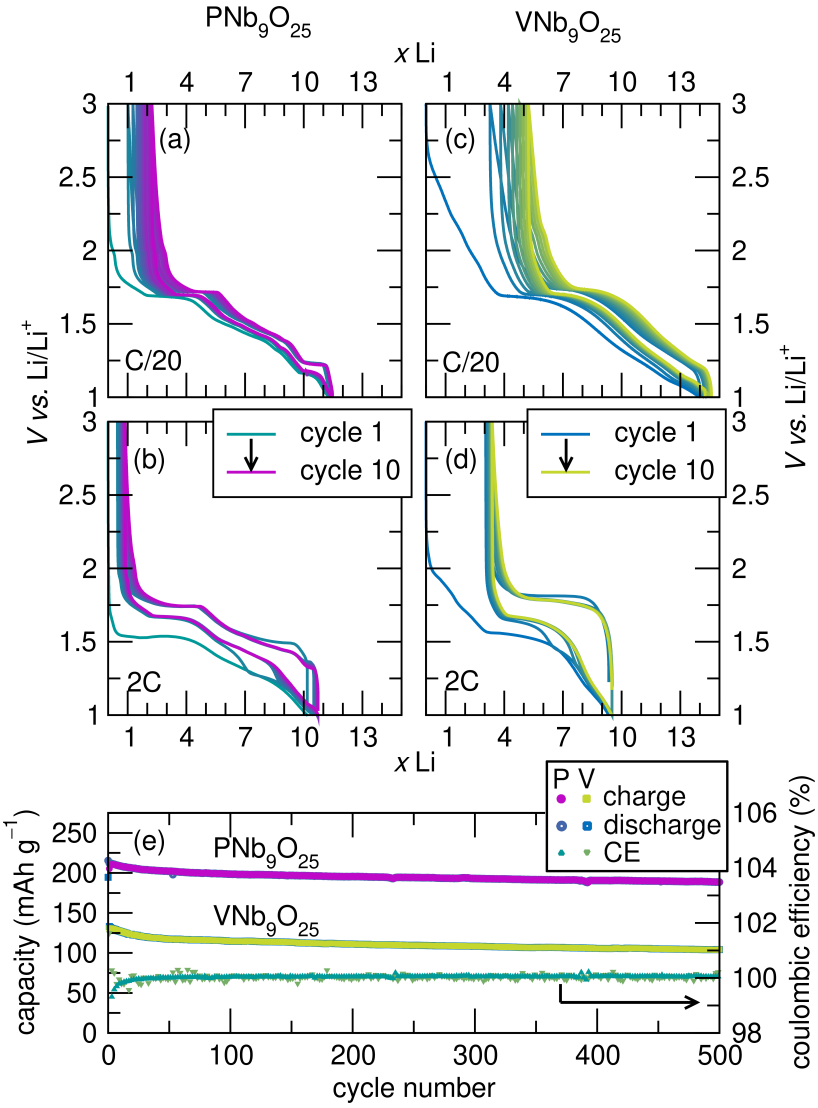

Figure 2: Cycling comparisons between PNb_9O_{25} and VNb_9O_{25} at slow and fast rates, as well as long-term cycling. (a) PNb_9O_{25} cycled at C/20 over 10 cycles shows its distinct plateau and reversible cycling. (b) PNb_9O_{25} cycled at 2C still maintains the same structure in the electrochemical curve with more polarization and slightly reduced Li incorporation. (c) VNb_9O_{25} cycled at C/20 shows the irreversible capacity loss on the first cycle equivalent to about 4 Li, then less capacity fade thereafter. (d) VNb_9O_{25} cycled at 2C still has the same capacity loss now equivalent to about 3 Li and a large increase in polarization. Li incorporation in VNb_9O_{25} is significantly reduced at 2C. (e) Long-term cycling comparison between PNb_9O_{25} and VNb_9O_{25} at 2C. Both show relatively high capacity retention, though PNb_9O_{25} maintains higher reversible capacity over 500 cycles.

the large irreversible capacity on the first discharge and greatly increased polarization. When cycled at 2C long-term, both have high capacity retention over 500 cycles, though interestingly PNb_9O_{25} maintains much higher capacity than VNb_9O_{25} by almost a factor

of two (190 mAhg^{-1} versus 100 mAhg^{-1} at the 500th cycle, respectively), as seen in Figure 1(e).

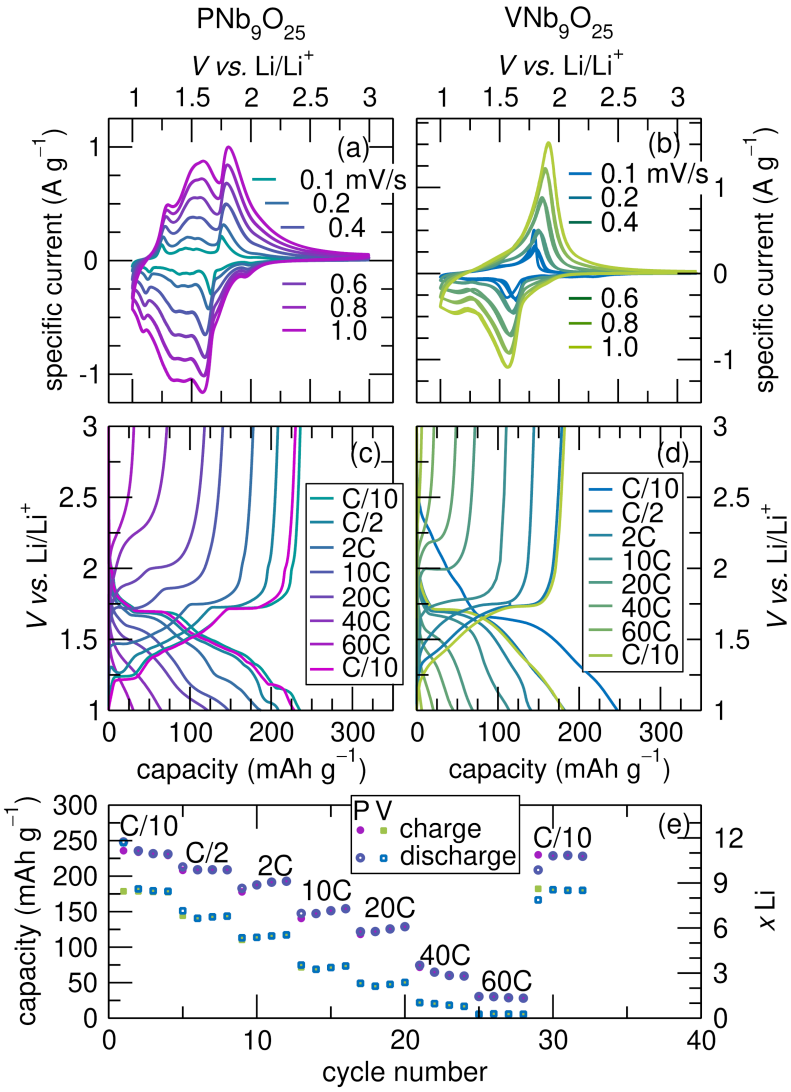

Figure 3: Variable rate electrochemistry comparison of PNb_9O_{25} and VNb_9O_{25}. (a) Cyclic voltammetry performed at sweep rates from 0.1 mVs^{-1} to 1.0 mVs^{-1} allows for analysis of the value of the exponent b for PNb_9O_{25}. (b) Cyclic voltammetry performed at sweep rates from 0.1 mVs^{-1} to 1.0 mVs^{-1} allows for b to be evaluated for VNb_9O_{25}. (c) PNb_9O_{25} cycled galvanostatically from C/10 to 60C, and its recovery. The second cycle (out of four for each rate) is shown for clarity. (d) VNb_9O_{25} cycled galvanostatically from C/10 to 60C, and its recovery. The first and second cycles are shown for C/10, but the second cycle is shown thereafter to see the evolution of the curves. (e) Cycle number versus capacity corresponding to the variable rate galvanostatic cycling depicted in (b) and (d). PNb_9O_{25} consistently shows higher capacity after the first discharge. Both PNb_9O_{25} and VNb_9O_{25} recover to almost their starting C/10 capacities.

Cyclic voltammetry at varying rates makes the underlying kinetic differences more apparent. Multiple redox processes can be teased out in the CV curve of PNb_9O_{25} from 1 V to 3 V, whereas there is only one distinct redox reaction revealed in the CV curve of VNb_9O_{25}. Varying the rates allow values of the exponent b to be calculated for each of these processes, which reveals which redox reactions are bulk- or surface-limited according to the power law relationship $I_p = av^b$, where I_p is the peak current, v the voltage sweep rate and a and b are fitting parameters.[54–56]

Values of the exponent b calculated for different peaks in the CV of PNb_9O_{25} and VNb_9O_{25} are presented in Table 1, and the calculations for these values in Figures S6 and S7 and Table S1. Both b-values calculated for the reduction and oxidation reactions in VNb_9O_{25} are closer to 0.5, suggesting diffusion-limited processes are associated with the bulk of the material. Conversely, PNb_9O_{25} has four distinct redox reactions, and while the high voltage reduction and oxidation peaks suggest diffusion limitations in the bulk, the redox reactions between 1.37 V and 1.57 V appear to be associated with the diffusion-limiting steps associated with the surface. It is important to distinguish that both PNb_9O_{25} and VNb_9O_{25} behave as battery materials, and not pseudocapacitors, as evidenced through the phase changes that occur in their diffraction patterns during cycling (Figure S8).[29] Overall, the b-value analysis lends quantitative insight into the improved rate capabilities in PNb_9O_{25} over VNb_9O_{25}.

Table 1: Quantitative insight into the kinetic variations between PNb_9O_{25} and VNb_9O_{25} is gleaned from varying the cyclic voltammetry sweep rate [Figure 3(a) and (b), and Figure S6 and S7]. Values of the exponent b for the four distinguishable peaks in the PNb_9O_{25} CV curve upon oxidation and reduction, and the one observable, reversible peak in the VNb_9O_{25} CV curve are listed for comparison.

	reduction		oxidation	
	position	b	position	b
PNb_9O_{25}	1.11 V	0.80	1.28 V	0.56
	1.37 V	0.95	1.49 V	0.91
	1.46 V	0.97	1.57 V	0.94
	1.62 V	0.62	1.79 V	0.70
VNb_9O_{25}	1.56 V	0.59	1.93 V	0.69

Both compounds exhibit impressive rate capabilities, with measurable capacity up to 60C, and more than 99% recovery of capacity when the rate is reduced back to C/10. This demonstrates a wide range of practical applications for electric vehicles and portable electronics, in which one may wish to discharge their batteries slowly but charge them within minutes. In this instance PNb_9O_{25} can reach 85% of its C/10 capacity in 30 minutes or 67% in 6 minutes. The surprising result from comparing the rate capabilities between PNb_9O_{25} and VNb_9O_{25} is that we would expect VNb_9O_{25}, if anything, to exhibit higher capacity given the higher ratio of redox active atoms per formula unit. However, the rate capabilities of PNb_9O_{25} far exceed those of VNb_9O_{25}. For example, at 2C, PNb_9O_{25} exhibits an additional 77 $mAhg^{-1}$ capacity than VNb_9O_{25}. Further, at 60C the capacity of VNb_9O_{25} diminished to almost zero, while in PNb_9O_{25} it is still 30 $mAhg^{-1}$. This wide range in performance given the very small chemical variations in these structures points to significant mechanistic differences in their redox properties.

Characterization of multielectron redox

Operando Nb K-edge X-ray absorption spectroscopy, especially the near edge region shown in Figure 4(a) and (c), lends insight into the reversibility of the niobium redox throughout the first cycle. The overall spectra and changes observed throughout the first cycle of PNb_9O_{25} and VNb_9O_{25} look similar, as expected for isostructural compounds. Both show a slight pre-edge feature in the pristine material centered at 18990 eV that is reversible once the material is re-oxidized. They both also show the same restructuring of the peak after the energy onset that shows a shift to lower energy upon reduction, which is restored to its position in the pristine state upon re-odixation.

The relationship between composition and the associated change in energy yields mechanistic information about how niobium is reduced and oxidized in both structures and highlights their differences. With PNb_9O_{25}, both the reduction and oxidation result in a single linear relationship between the composition and energy. This is the expected

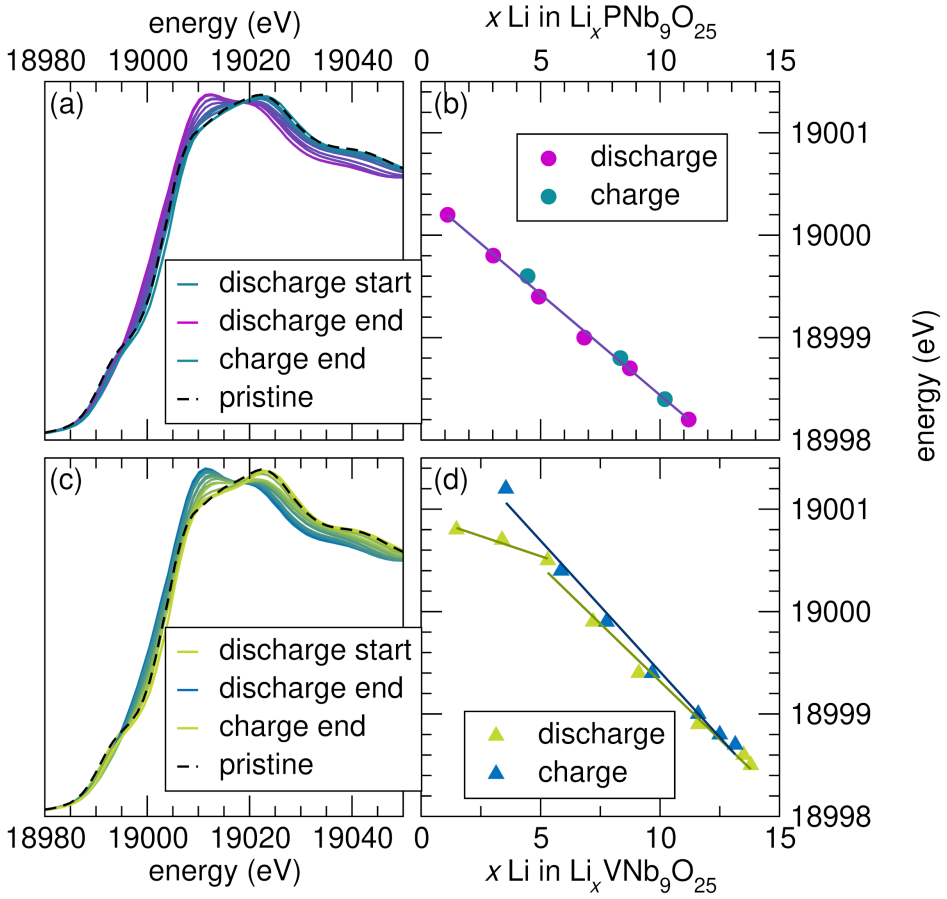

Figure 4: (a) Evolution of the XANES region of the Nb K-edge as PNb_9O_{25} is reduced to 1 V and subsequently oxidized to 3 V (one full cycle). (b) The energy change of the onset after the pre-edge region as a function of composition as Li is inserted into PNb_9O_{25}. There is a linear relationship upon discharge and charge. (c) Evolution of the XANES region of the Nb K-edge as VNb_9O_{25} is reduced to 1 V and subsequently oxidized to 3 V (one full cycle). (d) The energy change of the onset after the pre-edge region as a function of composition as Li is inserted into VNb_9O_{25}. In contrast with what is seen for PNb_9O_{25}, the initial change in energy VNb_9O_{29} is slower upon discharge, marked by a linear relationship with a shallower slope.

result for a single redox active element, which is continually being reduced at the same rate throughout discharge and subsequent charge. VNb_9O_{25} shows different trends, owing to the fact that vanadium is also redox active. While not probing the vanadium oxidation state directly, we can infer from the slow initial reduction of Nb up to $Li_5VNb_9O_{25}$ that vanadium is simultaneously being reduced during this stage of irreversible capacity loss [Figure S9]. Interestingly, there is still some reduction in niobium until this point, which

differs from the hypotheses in previous reports. It was earlier believed that only vanadium is initially reduced, linked to the irreversible capacity loss observed in VNb_9O_{25} in the first discharge. It is likely that the irreversible reduction of not only vanadium but also niobium is responsible for the diminished rate capabilities and capacity retention in VNb_9O_{25}.

We have employed *ex situ* XPS to quantitatively track the changes in oxidation states in niobium, phosphorus, and vanadium in both structures. The lithiated states were chosen based on clear changes in the galvanostatic response, such as before and after the discernible plateau [Figure 5(a) and (d)]. While XPS is quantitative and the measurements were done using air-free transfer from a glovebox, slight surface oxidation is still likely, skewing the results slightly toward Nb^{5+}. As expected, in the pristine state niobium only exists in the Nb^{5+} state [Figures 5(b), S13]. Even at the very beginning of lithiation with only 0.06 Li, 4% of niobium are converted to Nb^{4+}. This increases incrementally to 21% Nb^{4+} through x=1.4. At the end of the largest plateau, experimentally corresponding to x=4, 7% of niobium are converted to Nb^{3+}, but still a significant amount exists as Nb^{5+}. An interesting shift occurs in the sloping region between x=4 and x=9.4, in which the percentage of Nb^{3+} is almost 3 times that of Nb^{4+} (33% Nb^{3+} versus 13% Nb^{4+}). This indicates a complex mechanism in which either Nb^{5+} directly converts to Nb^{3+} or quickly reduces through Nb^{4+} to Nb^{3+}. Either way, Nb^{3+} is the favored reduced state toward the end of the discharge. After the final plateau at the end of discharge when x=11.2, an increase in Nb^{4+} is observed, such that 25% is Nb^{4+} and 29% is Nb^{3+}. Finally, upon charge, almost all of the niobium is oxidized back to Nb^{5+}, with only 2% remaining in the reduced Nb^{4+} state. Complete oxidation back to Nb^{5+} leads to the high capacity retention observed in PNb_9O_{25}.

To confirm that phosphorus does not participate in redox, high resolution XPS was measured in the P 2*p* region as well [Figure 5(c)]. Though the signal-to-noise ratio is diminished due to phosphorus being lighter and in much lower abundance than niobium in the sample, there is no emergence of a new signal to indicate that phosphorus is being

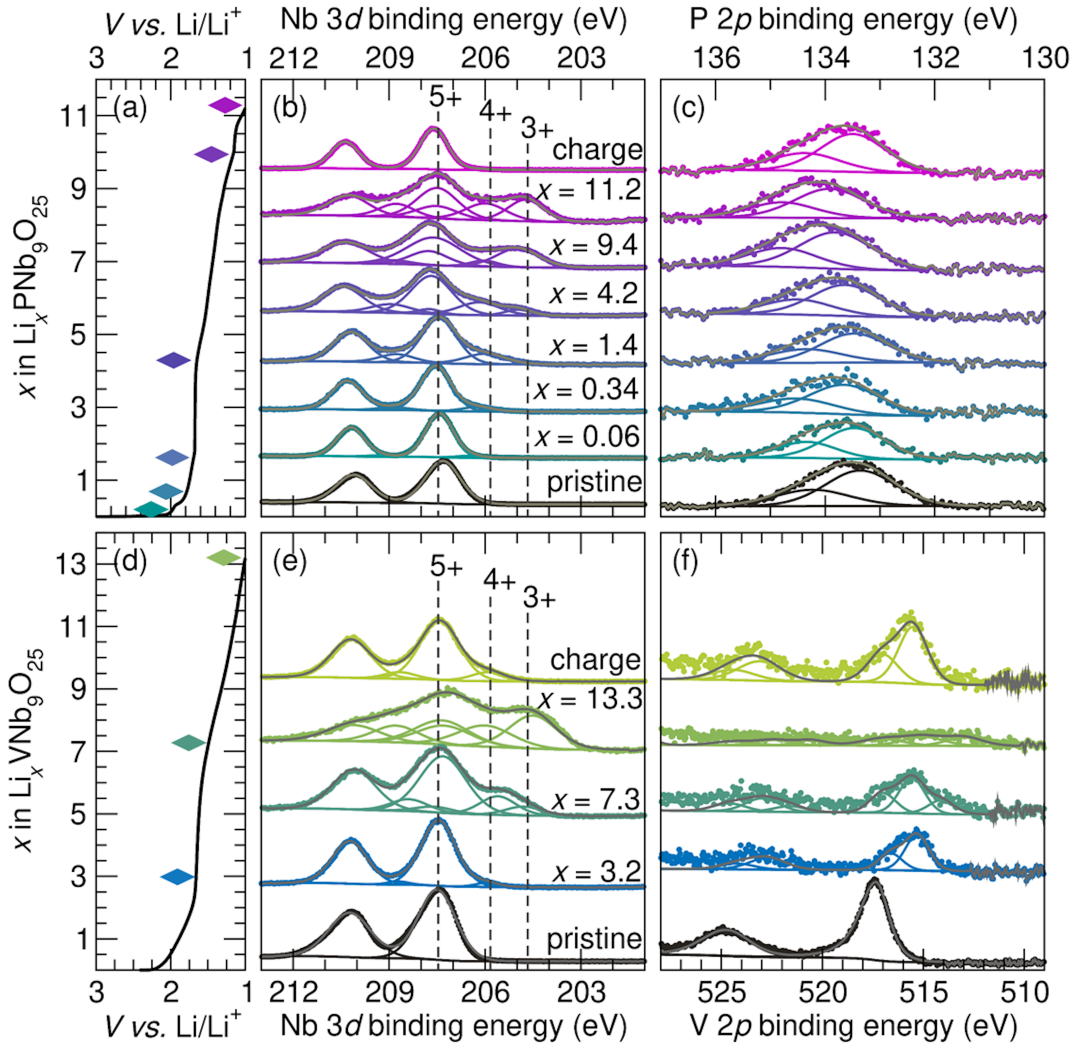

Figure 5: (a) The first galvanostatic discharge for Li insertion in PNb_9O_{25} and the states of charge corresponding to the XPS spectra in the Nb 3*d* binding energy region (b) and P 2*p* binding energy region (c). Similarly, (d) is the VNb_9O_{25} first galvanostatic discharge annotated to indicate the states of charge reflected in the Nb 3*d* region (e) and V 2*p* region (f). The oxidation state assignments were made using both literature references as well as Nb_2O_5, NbO_2, and NbO references collected on the same spectrometer. The duplication of peaks arises from spin-orbit splitting – the Nb 3*d* states split into Nb $3d_{\frac{5}{2}}$ (lower binding energy) and Nb $3d_{\frac{3}{2}}$ (higher binding energy). This is the case for V 2*p* and P 2*p* splitting into $2p_{\frac{3}{2}}$ (lower binding energy) and $2p_{\frac{1}{2}}$ (higher binding energy). For clarity, only the $3d_{\frac{5}{2}}$ and $2p_{\frac{3}{2}}$ peaks are marked. The grey line on each spectrum is the total fit arising from the peaks fitted to each oxidation state.

reduced during discharge.

High resolution XPS of VNb_9O_{25} lends insight into the electrochemical processes in this crystal structure, as well. Previous reports have speculated through XRD and limited XPS of

Table 2: Quantitative analysis of the evolution of oxidation states from fitting the high resolution spectra found in Figure 5.

$Li_xPNb_9O_{25}$				
x in $Li_xPNb_9O_{25}$	% Nb^{5+}	% Nb^{4+}	% Nb^{3+}	average
0.06	96	4	0	4.95
0.34	91	9	0	4.91
1.40	79	21	0	4.79
4.00	70	23	7	4.62
9.40	54	13	33	4.20
11.2	46	25	29	4.18
charged to 3.0 V	98	2	0	4.98

$Li_xVNb_9O_{25}$				
x in $Li_xVNb_9O_{25}$	% Nb^{5+}	% Nb^{4+}	% Nb^{3+}	average
3.50	96	4	0	4.96
7.30	72	19	9	4.38
13.3	32	29	39	3.93
charged to 3.0 V	88	12	0	4.88

VNb_9O_{25} that the irreversible capacity in the first discharge is due to irreversible reduction of V^{5+} to V^{3+}. However, this is only partly the case. There is irreversible capacity loss due to both incomplete oxidation of niobium back to Nb^{5+} and vanadium back to V^{5+} [Figures 5(e),(f) and S14 and S15]. Approximately 12% of the niobium remains as Nb^{4+} at the end of charge. The low signal-to-noise ratio of the vanadium binding energy region prevents the same quantitative analysis with confidence, especially at the bottom of discharge when the total intensity is broadened by all three oxidation states, but a non-trivial fraction of vanadium oxidizes completely to V^{5+}. The largest fraction remains as V^{4+}, though this is still oxidized as compared to when VNb_9O_{25} is most lithiated [Figure S15]. Quantitative analysis of the percentages of oxidation states arising from fitting the spectra can be found in Table 2. It is likely that the irreversibility due to niobium is the driving force for the larger capacity loss over extended cycling, since niobium comprises the majority of the structure, though this is conjecture. When evaluated with the significant differences in the galvanostatic behavior between PNb_9O_{25} and VNb_9O_{25}, the small chemical difference of replacing phosphorus with vanadium in low overall concentration leads to surprisingly large

mechanistic deviations in an otherwise identical crystal structure, which has implications for future design of new complex oxides for electrode materials.

Evidence of an insulator-to-metal transition in $Li_xPNb_9O_{25}$

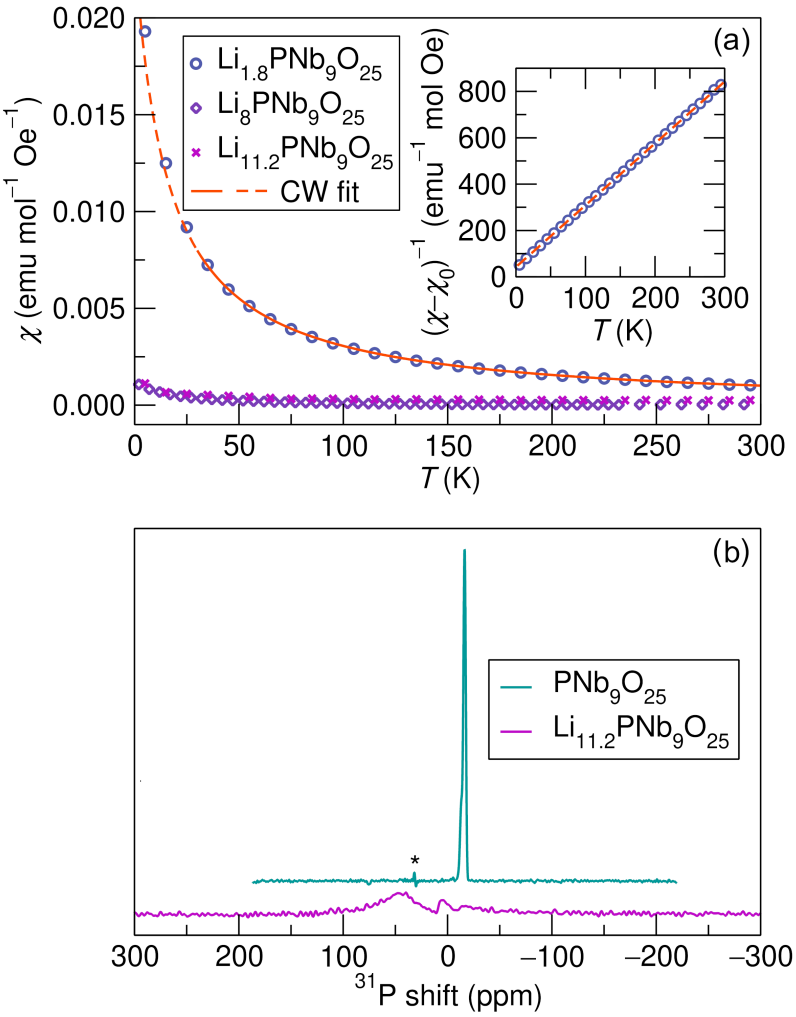

Figure 6: (a) magnetic susceptibility *vs.* temperature for three samples. $Li_{1.8}PNb_9O_{25}$, a lightly-lithiated sample, shows Curie-Weiss (CW) paramagnetism consistent with the localization of the Nb d-electrons into discrete magnetic moments. The Curie-Weiss fit shown is performed between 30 K and 300 K, and extrapolated to lower temperatures. The heavily-lithiated $Li_8PNb_9O_{25}$ and $Li_{11.2}PNb_9O_{25}$ samples, on the other hand, show much lower susceptibility and are not well-fit with the Curie-Weiss relation, consistent with delocalization of the d electrons. (b) ^{31}P NMR spectra of PNb_9O_{25} before cycling and fully lithiated at $Li_{11.2}PNb_9O_{25}$ (cycled to 1 V) both referenced to solid triphenylphosphine. The MAS speeds were respectively 30 kHz for PNb_9O_{25} and 25 kHz for $Li_{11.2}PNb_9O_{25}$.

Given the technical difficulties in carrying out reliable ex situ electrical transport measurements on the lithiated samples (described in detail in the Supporting Information), the potential insulator-to-metal transition in Li-inserted PNb_9O_{25} was probed using magnetis susceptibility measurements and solid-state NMR studies.

Figure 6(a) shows magnetic susceptibility as a function of temperature for $Li_{1.8}PNb_9O_{25}$, $Li_{8.0}PNb_9O_{25}$, and $Li_{11.2}PNb_9O_{25}$, expressed per mol formula unit. The lightly-lithiated sample ($x = 1.8$) shows a magnetic susceptibility χ that follows the Curie-Weiss law:

$$\chi = \frac{C}{T - \theta} + \chi_0 \tag{1}$$

where C is the Curie constant, T is the temperature, θ is the Weiss temperature, and χ_0 is the temperature-independent proportion of the magnetic susceptibility. Fitting the susceptibility between 30 K and 300 K to this equation yields $C = 0.375$ emu K mol^{-1} Oe^{-1}, $\theta = -15.9$ K, and $\chi_0 = -0.000177$ emu mol^{-1}Oe^{-1}. This value of C computes to a local paramagnetic moment $\mu_{\text{eff}} = 1.29\mu_B$ *per* inserted Li, which is in reasonable agreement for the theoretical value expected for a single Nb^{4+} ion ($\mu_{\text{eff}} = 1.55\,\mu_B$).[57] Therefore, this susceptibility data suggests a picture where, for low levels of lithiation, the electrons introduced by adding lithium to PNb_9O_{25} remain localized as discrete paramagnetic ion spins sitting on individual Nb atoms, rather than becoming delocalized into a metallic state. This mechanism points to why the introduction of electrons to the Nb d-band *via* lithiation does not, for low levels of lithiation, immediately result in a metal. Upon the introduction of larger quantities of Li ($x = 8.0$ and $x = 11.2$), this paramagnetic signal is greatly suppressed. Attempts to fit the susceptibility to the Curie-Weiss law resulted in poor fits with nonphysical parameters, and μ_{eff} values ≤ 0.2 per Li inserted. This loss of Curie-Weiss paramagnetism is consistent with the formation of metallic conducting state where the Nb d electrons now form a delocalized band instead of remaining in localized in paramagnetic moments. Furthermore, some temperature-independent paramagnetism is seen in these samples, consistent with the Pauli paramagnetism that occurs in systems with metal-

lic electrons. These susceptibility results are similar to those observed in the $Li_xTiNb_2O_7$ electrode system, which is also believed to become close to metallic upon lithiation.[24]

Figure 6(b) shows the 1D ^{31}P NMR spectrum of pristine PNb_9O_{25} and fully-lithiated $Li_{11.2}PNb_9O_{25}$. The signal in PNb_9O_{25} is relatively sharp, close to –15 ppm. The spectrum of $Li_{11.2}PNb_9O_{25}$, however, is dramatically different. The main chemical environment is shifted to 50 ppm and is much broader, spanning 75 ppm, suggestive of a Knight shift due to the delocalized electrons in the (metallic) compound, similar to what is observed in the ^7Li NMR spectrum upon delithiation in $LiCoO_2$.[19] A more complete temperature-dependent study of the Knight shift and NMR studies across the range of lithiation, in addition to ^7Li solid-state NMR studies would further strengthen these arguments, but the interpretation of the NMR spectra is consistent with the magnetic susceptibiility studies.

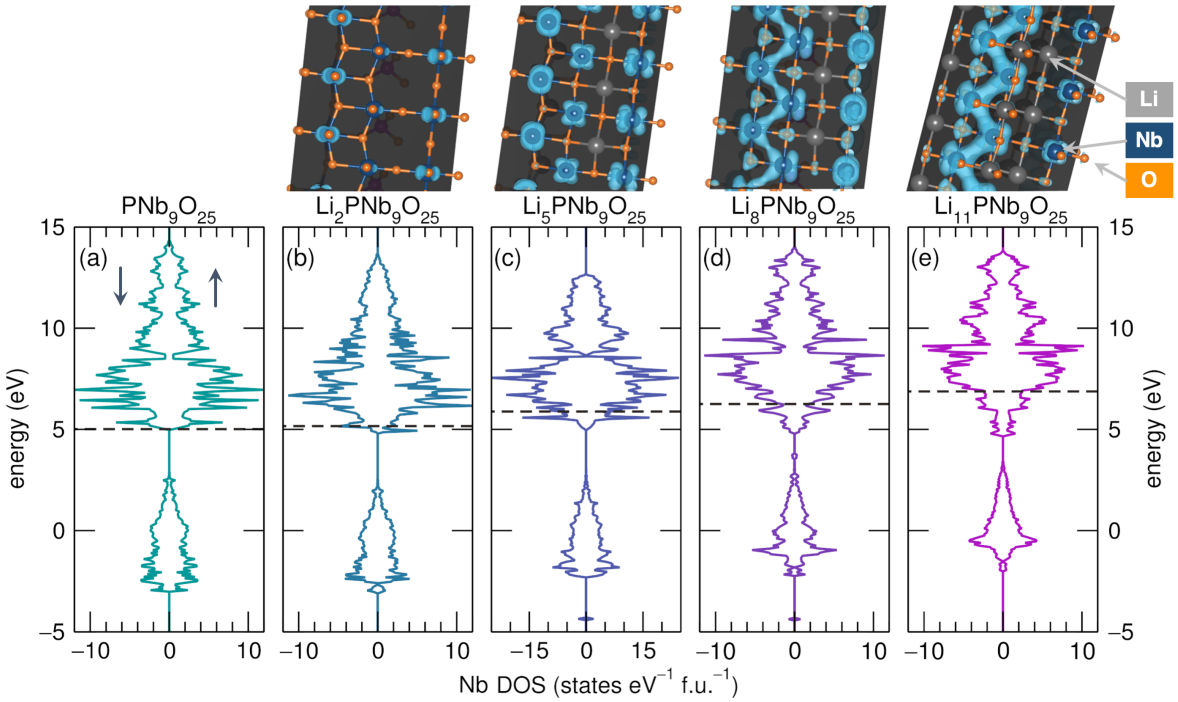

Figure 7: Nb partial densities of states (DOS) across various compositions of $Li_xPNb_9O_{25}$ and the corresponding structures and d-electron densities, showing Nb d states, which are empty in PNb_9O_{25} case but become occupied as the compound is lithiated. The charge densities correspond to electronic states with energies that extend from the bottom of the d block up to the Fermi level. In each DOS panel, majority spin states are depicted in the right panel, and minority states in the left. In the upper panels, the P atoms are magenta and in the background.

Electron delocalization at high states of lithiation can be best visualized by separating the crystal structure into distinct regions of structural features and Nb t_{2_g} state density. PNb_9O_{25} has three symmetrically nonequivalent niobium in its unit cell. Two form NbO_6 octahedral units that are edge sharing with the octahedra in the blocks above and below them. These units merely differ by one octahedra sharing a corner with phosphorous and the other not. These octahedral units connect the blocks along the infinite axis through their edges forming a jagged network of NbO_6 octahedral units. There is also a single niobium that forms an NbO_6 octahedra where the oxygens are shared only along octahedral vertices. Edge- and vertex-sharing octahedra exhibit large differences in d-orbital overlap, and in both cases, the bonding changes dramatically with composition.

$Li_xPNb_9O_{25}$ starts as a d^0 band insulator prior to lithiation ($x = 0$). From the partial Nb t_{2_g} state density plots (Figure 7), at low lithium composition we observe little d orbital overlap. This is a result of the electrons occupying t_{2_g} orbitals, effectively preventing orbital overlap and therefore, delocalization. At this stage, we anticipate that electron-electron correlation (not described here) would be important, forcing the d electron to remain localized into discrete spins on Nb ions, as is also seen in the magnetic susceptibility data. In this picture, any electrical transport would require a hopping mechanism,[58] which would result in the thermally-activated conduction. As the lithium composition increases, d orbital overlap between the edge-sharing octahedra increases as electrons further fill t_{2_g} orbitals. This occurs along the edge-sharing connections, allowing a network of electronic conductivity through the length of the crystal [Figure 7(d) and (e)]. The transition from no orbital overlap between the edge-sharing octahedra and electronic conductivity between them appears to initially occur at $Li_5PNb_9O_{25}$ [Figure 7(c)], and increases further in the $Li_8PNb_9O_{25}$ configuration, where the electronic density begins to emerge along the oxygen atoms [Figure 7(d)]. This effect is amplified when the composition reaches over $x = 11$ for the $Li_xPNb_9O_{25}$ system, where there is a large increase in the electronic density of the edge-sharing octahedra [Figure 7(e)]. The evolution described here is consisted with all of

the experimental observations, notably the magnetic susceptibility, NMR, the impedance shown in the SI, and the sample color changes.

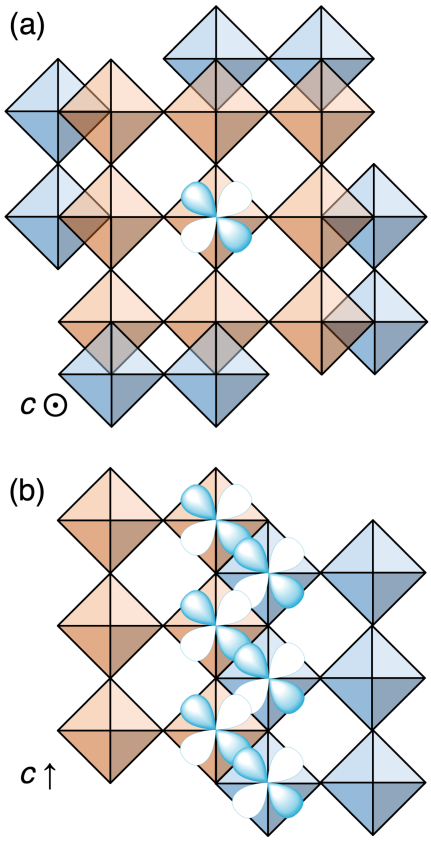

Figure 8: Schematic of (a) the initial localization of electron density on a t_{2g} orbital on an octahedron that is only corner-connected with other octahedra, and (b) delocalized electron density extended along edge-sharing regions as a result of t_{2g} being able to communicate with each other through the shared octahedral edges. This takes place at higher levels of lithiation.

Along the vertex sharing octahedra, there is charge localization on the niobium at low lithium compositions. Since electrons fill the t_{2g} orbital, there is no d orbital overlap with surrounding octahedra. The electron density in corner-sharing and edge-sharing regions is conveyed with greater clarity in the schematic representation in Figure 8. Localization of electrons near the vertex-sharing octahedra was also found for other Wadsley-Roth structures including $Nb_{14}W_3O_{44}$, $Nb_{16}W_5O_{55}$, and $Nb_{12}WO_{36}$,[25] suggesting similarities in electronic conductivity and charge localization among crystallographic shear structures.

For higher compositions, the electron density on the vertex-sharing octahedra appears to decrease with increasing composition and instead is mainly present on the edge-sharing octahedra for lithium compositions over $x = 8$ in $Li_xPNb_9O_{25}$. A detailed first-principles thermodynamics study of the crystal and electronic structure evolution with Li insertion in PNb_9O_{25} is forthcoming.

Summary of the complex processes in PNb_9O_{25}

A summary of the discussed, complex processes occurring throughout the PNb_9O_{25} discharge curve is shown in Figure 9. Niobium oxidation states are tracked using a combination of XANES and XPS. Initially, Nb is reduced from Nb^{5+} to Nb^{4+} as up to 2 Li are inserted. After the first extended plateau at 1.72 V, the evolution of Nb^{3+} is observed, signaling multielectron redox properties. Through the sloping region up to $Li_{10}PNb_9O_{25}$, there is a sharp increase in the percentage of Nb^{3+}, surpassing the amount of Nb^{4+}. This suggests that Nb^{5+} is being reduced to Nb^{3+} either directly or moving through Nb^{4+}. Finally, more Nb^{5+} is reduced through the end of discharge. Also mapped onto the discharge curve is where the expected insulator-to-metal transition occurs based on a combination of experimental measurements, the optical color change, and DFT calculations. At low levels of lithiation, the material remains insulating due localization of the electron density. At full lithiation, the material becomes metallic, and the density maps of the Nb t_{2_g} states reflect delocalization along the edge-sharing regions in the structure. From DFT, we can extrapolate that this delocalization occurs around $x = 5$. The color of the purely lithiated samples (no carbon or binder additives) reflects these changes in the electrical conductivity. The material changes from white in its pristine state to grey at very low levels of lithiation ($x = 0.06$). By $x = 0.33$, the material is blue, and at $x = 2$ the color deepens to a dark blue. Thereafter, and first observed at $x = 4.75$, the material is black, coinciding with the expected insulator-to-metal transition as a function of composition.

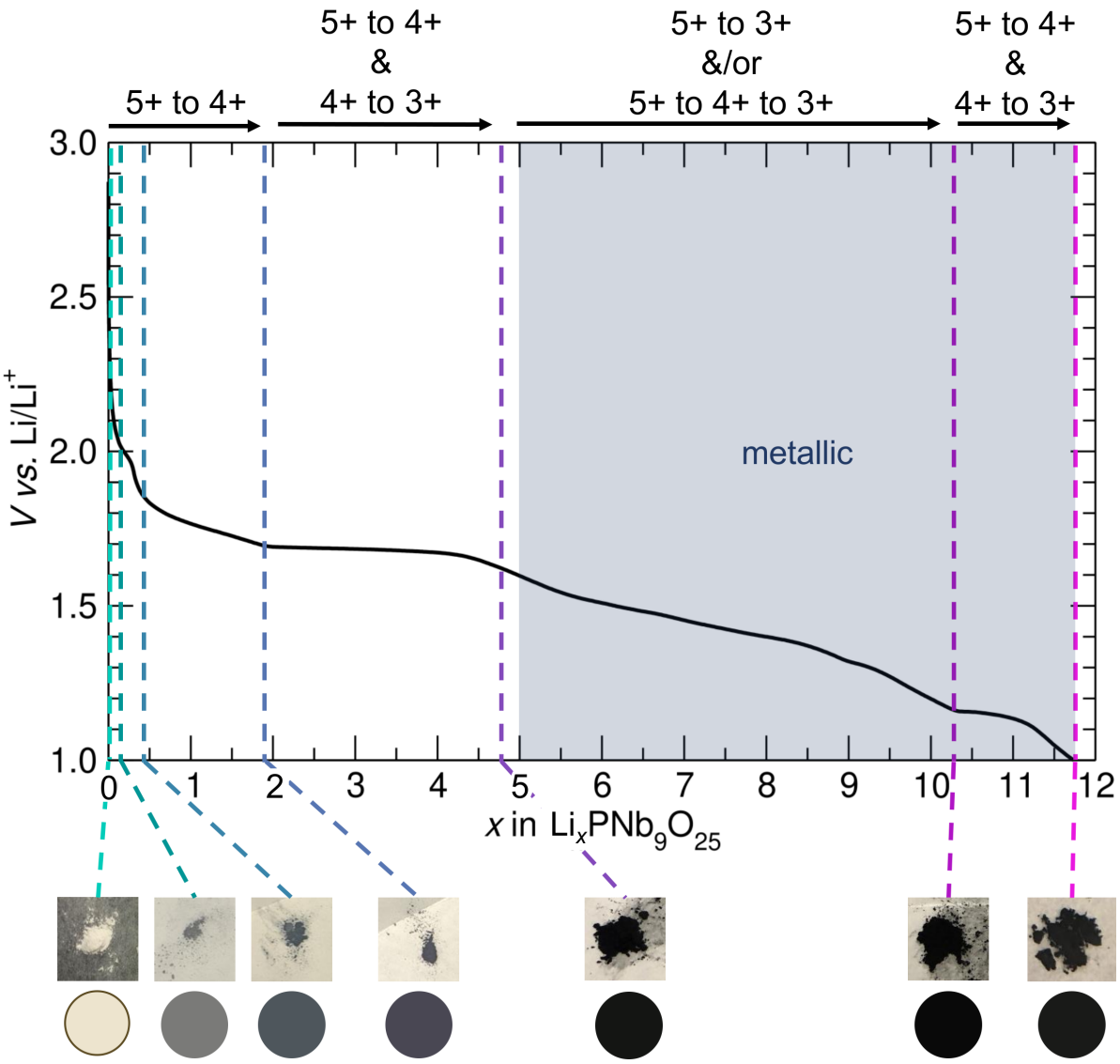

Figure 9: PNb_9O_{25} goes through a complicated redox mechanism that involves multielectron redox on Nb and induces an insulator-to-metal transition. The conversion from Nb^{5+} to Nb^{3+} is summarized on top of the discharge curve, and the color evolution as Li is progressively inserted from white, to grey, to blue, to black is shown at the bottom.

Conclusion

Electrochemical comparisons of PNb_9O_{25} and VNb_9O_{25}, particularly the use of variable rate testing, indicate very small amounts of chemical substitution can dramatically influence electrochemical behavior, diffusion kinetics, and cycling performance in the high-performing Wadsley-Roth family of fast-charging electrode materials. PNb_9O_{25} exhibits

impressive rate capabilities with observed capacity up to 60C and more than 1 electron stored per transition metal, leading to its high capacity retention over hundreds of cycles. Additionally, we directly observe an insulator-to-metal transition in the material, which is highly desirable for applications and likely contributes to its fast rate capabilities in micron-sized particles. Irreversible reduction of vanadium and niobium in VNb_9O_{25} results in lower capacity retention and contributes to its comparably sluggish rate capabilities as compared to PNb_9O_{25}, exemplifying that not all shear structures are created equally for Li insertion. Chemical tuning of this structure type and other structure types within the broader crystallographic shear structure family may allow for optimization of the electrochemical features observed.

Supporting Information Available

X-ray diffraction Rietveld fits and scanning electron micrographs of the samples described here prior to lithiation, electrochemical and battery cycling data including replicate cells, *b*-value analysis, cycling data corresponding to the *operando* XAS data, *operando* XRD data of the two compounds as they are lithiated and delithiated, XPS data, including standards, and temperature-dependent impedance studies on lithiated PNb_9O_{25} samples.

Acknowledgement

This work was supported as part of the Center for Synthetic Control Across Length-scales for Advancing Rechargeables (SCALAR), an Energy Frontier Research Center funded by the U.S. Department of Energy, Office of Science, Basic Energy Sciences under Award # DE-SC0019381.The research reported here made use of shared facilities of the UC Santa Barbara Materials Research Science and Engineering Center (MRSEC, NSF DMR 1720256), a member of the Materials Research Facilities Network (www.mrfn.org). XAS data was col-

lected at the X-ray Science Division beamline 12-BM and diffraction data was collected at beamlines 11-BM and 17-BM at the Advanced Photon Source, Argonne National Laboratory, a U.S. Department of Energy (DOE) Office of Science User Facility operated for the DOE Office of Science by Argonne National Laboratory under Contract No. DE-AC02-06CH11357. We gratefully acknowledge help from Dr. Sungsik Lee at beamline 12-BM for help with data collection and Dr. Kamila Wiaderek for help with setting up the electrochemistry at beamline 12-BM. We also thank Dr. Johanna Nelson Weker at the Stanford Synchrotron Radiation Lightsource for helpful discussions regarding XAS data processing and Dr. Peter Richardson at UC Santa Barbara for helpful discussions regarding NMR.

References

(1) Goodenough, J. B.; Park, K. S. The Li-Ion Rechargeable Battery: A Perspective. *J. Am. Chem. Soc.* **2013**, *135*, 1167–1176.

(2) Jiang, J.; Chen, J.; Dahn, J. R. Comparison of the Reactions Between $Li_{7/3}Ti_{5/3}O_4$ or LiC_6 and Nonaqueous Solvents or Electrolytes Using Accelerating Rate Calorimetry. *J. Electrochem. Soc.* **2004**, *151*, 2082–2087.

(3) Jiang, J.; Dahn, J. R. Dependence of the Heat of Reaction of $Li_{0.81}C_6$ (0.1 V), $Li_7Ti_5O_{12}$ (1.55 V), and $Li_{0.5}VO_2$ (2.45 V) Reacting with Nonaqueous Solvents or Electrolytes on the Average Potential of the Electrode Material. *J. Electrochem. Soc.* **2006**, *153*, 310–315.

(4) Vetter, J.; Novák, P.; Wagner, M. R.; Veit, C.; Möller, K. C.; Besenhard, J. O.; Winter, M.; Wohlfahrt-Mehrens, M.; Vogler, C.; Hammouche, A. Ageing Mechanisms in Lithium-Ion Batteries. *J. Power Sources* **2005**, *147*, 269–281.

(5) Downie, L. E.; Krause, L. J.; Burns, J. C.; Jensen, L. D.; Chevrier, V. L.; Dahn, J. R. In situ Detection of Lithium Plating on Graphite Electrodes by Electrochemical Calorimetry. *J. Electrochem. Soc.* **2013**, *160*, 588–594.

(6) Burns, J. C.; Stevens, D. A.; Dahn, J. R. In-situ Detection of Lithium Plating Using High Precision Coulometry. *J. Electrochem. Soc.* **2015**, *162*, A959–A964.

(7) Ribière, P.; Grugeon, S.; Morcrette, M.; Boyanov, S.; Laruelle, S.; Marlair, G. Investigation on the Fire-Induced Hazards of Li-Ion Battery Cells by Fire Calorimetry. *Energy Environ. Sci.* **2012**, *5*, 5271–5280.

(8) Zhao, K.; Pharr, M.; Vlassak, J. J.; Suo, Z. Fracture of Electrodes in Lithium-Ion Batteries Caused by Fast Charging. *J. Appl. Phys.* **2010**, *108*, 1–7.

(9) Palacín, M. R.; Simon, P.; Tarascon, J. M. Nanomaterials for Electrochemical Energy Storage: the Good and the Bad. *Acta Chim. Slov.* **2016**, 417–423.

(10) Kang, B.; Ceder, G. Battery Materials for Ultrafast Charging and Discharging. *Nature* **2009**, *458*, 190–193.

(11) Lukatskaya, M. R.; Dunn, B.; Gogotsi, Y. Multidimensional Materials and Device Architectures for Future Hybrid Energy Storage. *Nat. Commun.* **2016**, *7*, 1–13.

(12) Yang, Z.; Choi, D.; Kerisit, S.; Rosso, K. M.; Wang, D.; Zhang, J.; Graff, G.; Liu, J. Nanostructures and Lithium Electrochemical Reactivity of Lithium Titanites and Titanium Oxides: A Review. *J. Power Sources* **2009**, *192*, 588–598.

(13) Haetge, J.; Hartmann, P.; Brezesinski, K.; Janek, J.; Brezesinski, T. Ordered Large-Pore Mesoporous $Li_4Ti_5O_{12}$ Spinel Thin Film Electrodes with Nanocrystalline Framework for High Rate Rechargeable Lithium Batteries: Relationships Among Charge Storage, Electrical Conductivity, and Nanoscale Structure. *Chem. Mater.* **2011**, *23*, 4384–4393.

(14) Odziomek, M.; Chaput, F.; Rutkowska, A.; Świerczek, K.; Olszewska, D.; Sitarz, M.; Lerouge, F.; Parola, S. Hierarchically Structured Lithium Titanate for Ultrafast Charging in Long-Life High Capacity Batteries. *Nat. Commun.* **2017**, *8*, 1–7.

(15) Yamamoto, L. N. Zero-Strain Insertion Material of $Li[Li_{1/3}Ti_{5/3}]O_4$ for Rechargeable Lithium Cells. *J. Electrochem. Soc.* **1995**, *142*, 1431–1435.

(16) Kim, C.; Norberg, N. S.; Alexander, C. T.; Kostecki, R.; Cabana, J. Mechanism of Phase Propagation During Lithiation in Carbon-Free $Li_4Ti_5O_{12}$ Battery Electrodes. *Adv. Funct. Mater.* **2013**, *23*, 1214–1222.

(17) Song, M. S.; Benayad, A.; Choi, Y. M.; Park, K. S. Does $Li_4Ti_5O_{12}$ Need Carbon in

Lithium Ion Batteries? Carbon-Free Electrode with Exceptionally High Electrode Capacity. *Chem. Commun.* **2012**, *48*, 516–518.

(18) Mizushima, K.; Jones, P.; Wiseman, P.; Goodenough, J. Li_xCoO_2: A New Cathode Material for Batteries of High Energy Density. *Solid State Ionics* **1981**, *3-4*, 171–174.

(19) Menétriér, M.; Saadoune, I.; Levasseur, S.; Delmas, C. The Insulator–Metal Transition Upon Lithium Deintercalation from $LiCoO_2$: Electronic Properties and ^{7}Li NMR Study. *J. Mater. Chem.* **1999**, *9*, 1135–1140.

(20) Ensling, D.; Thissen, A.; Laubach, S.; Schmidt, P. C.; Jaegermann, W. Electronic structure of $LiCoO_2$ Thin Films: A Combined Photoemission Spectroscopy and Density Functional Theory Study. *Phys. Rev. B* **2010**, *82*, 1–16.

(21) Griffith, K. J.; Forse, A. C.; Griffin, J. M.; Grey, C. P. High-Rate Intercalation without Nanostructuring in Metastable Nb_2O_5 Bronze Phases. *J. Am. Chem. Soc.* **2016**, *138*, 8888–8899.

(22) Griffith, K. J.; Wiaderek, K. M.; Cibin, G.; Marbella, L. E.; Grey, C. P. Niobium Tungsten Oxides for High-Rate Lithium-Ion Energy Storage. *Nature* **2018**, *559*, 556–563.

(23) Deng, Q.; Fu, Y.; Zhu, C.; Yu, Y. Niobium-Based Oxides Toward Advanced Electrochemical Energy Storage: Recent Advances and Challenges. *Small* **2019**, *15*, 1–26.

(24) Griffith, K. J.; Seymour, I. D.; Hope, M. A.; Butala, M. M.; Lamontagne, L. K.; Preefer, M. B.; Koçer, C. P.; Henkelman, G.; Morris, A. J.; Cliffe, M. J.; Dutton, S. E.; Grey, C. P. Ionic and Electronic Conduction in $TiNb_2O_7$. *J. Am. Chem. Soc.* **2019**, *141*, 16706–16725.

(25) Koçer, C. P.; Griffith, K. J.; Grey, C. P.; Morris, A. J. Cation Disorder and Lithium Insertion Mechanism of Wadsley-Roth Crystallographic Shear Phases from First Principles. *J. Am. Chem. Soc.* **2019**, *141*, 15121–15134.

(26) Cava, R. J.; Santoro, A.; Murphy, D. W.; Zahurak, S. M.; Roth, R. S. The Structures of the Lithium Inserted Metal oxides $Li_{0.2}ReO_3$ and $Li_{0.36}WO_3$. *J. Solid State Chem.* **1983**, *50*, 121–128.

(27) Bashian, N. H.; Zhou, S.; Zuba, M.; Ganose, A. M.; Stiles, J. W.; Ee, A.; Ashby, D. S.; Scanlon, D. O.; Piper, L. F.; Dunn, B.; Melot, B. C. Correlated Polyhedral Rotations in the Absence of Polarons During Electrochemical Insertion of Lithium in ReO_3. *ACS Energy Lett.* **2018**, *3*, 2513–2519.

(28) Guo, B.; Yu, X.; Sun, X. G.; Chi, M.; Qiao, Z. A.; Liu, J.; Hu, Y. S.; Yang, X. Q.; Goodenough, J. B.; Dai, S. A Long-Life Lithium-Ion Battery with a Highly Porous $TiNb_2O_7$ Anode for Large-Scale Electrical Energy Storage. *Energy Environ. Sci.* **2014**, *7*, 2220–2226.

(29) Patoux, S.; Dolle, M.; Rousse, G.; Masquelier, C. A Reversible Lithium Intercalation Process in an ReO_3-type structure PNb_9O_{25}. *J. Electrochem. Soc. A* **2002**, *149*, 391–400.

(30) Drozhzhin, O. A.; Vorotyntsev, M. A.; Maduar, S. R.; Khasanova, N. R.; Abakumov, A. M.; Antipov, E. V. Li-Ion Diffusion in $Li_xNb_9PO_{25}$. *Electrochim. Acta* **2013**, *89*, 262–269.

(31) Roth, R. S.; Wadsley, A. D.; Andersson, S. The Crystal Structure of PNb_9O_{25} ($P_2O_5{\cdot}9Nb_2O_5$). *Acta Crystallogr.* 643–647.

(32) Andersson, S.; Wadsley, A. Crystallographic Shear and Diffusion Paths in Certain Higher Oxides of Niobium, Tungsten, Molybdenum and Titanium. *Nature* **1966**, *211*, 581–583.

(33) Andersson, S. The Description of Non-Stoichiometric Transition Metal Oxides. A Logical Extension of Inorganic Crystallography. *Bull. Soc. Fr. Mineral. Cristallogr.* **1967**, *90*, 522–527.

(34) Andersson, S.; Galy, J. Wadsley Defects and Crystallographic Shear in Hexagonally Close-Packed Structures. *J. Solid State Chem.* **1970**, *1*, 576–582.

(35) Murphy, D. W.; Christian, P. A. Solid State Electrodes for High Energy Batteries. *Science* **1979**, *205*, 651–656.

(36) Murphy, D. W.; Greenblatt, M.; Cava, R. J.; Zahurak, S. M. Topotactic Lithium Reactions with ReO_3 Related Shear Structures. *Solid State Ionics* **1981**, *5*, 327–329.

(37) Cava, R. J.; Murphy, D. W.; Zahurak, S. M. Lithium Insertion in Wadsley-Roth Phases Based on Niobium Oxide. *J. Electrochem. Soc.* **1983**, *130*, 2345–2351.

(38) Wang, E.; Kimura, N.; Greenblatt, M. Lithium Insertion in $V_3Nb_9O_{29}$. A Wadsley-Roth Type Phase. *J. Electrochem. Soc.* **1985**, *132*, 1505–1506.

(39) Li, Y.; Sun, C.; Goodenough, J. B. Electrochemical Lithium Intercalation in Monoclinic $Nb_{12}O_{29}$. *Chem. Mater.* **2011**, *23*, 2292–2294.

(40) Levin, E. M.; Roth, R. S. The System Niobium Pentoxide-Phosphorus Pentoxide. *J. Solid State Chem.* **1970**, *2*, 250–261.

(41) Benabbas, A.; Borel, M. M.; Grandin, A.; Leclaire, A.; Raveau, B. Redetermination of the Structure of PNb_9O_{25}. *Acta Crystallogr. C* **1991**, *47*, 849–850.

(42) Waring, J.; Roth, R. Phase Equilibria in the V_2O_5–Nb_2O_5 System. *J. Res. Nat. Bur. Stand. A* **1965**, *69A*, 119–121.

(43) Nasri, R.; Chérif, S. F.; Zid, M. F.; Driss, A. β-Nb9VO25. *Acta Crystallogr. E* **2014**, *70*.

(44) Borkiewicz, O. J.; Shyam, B.; Wiaderek, K. M.; Kurtz, C.; Chupas, P. J.; Chapman, K. W. The AMPIX Electrochemical Cell: A Versatile Apparatus for In Situ X-Ray Scattering and Spectroscopic Measurements. *J. Appl. Crystallogr.* **2012**, *45*, 1261–1269.

(45) Ravel, B.; Newville, M. ATHENA, ARTEMIS, HEPHAESTUS: Data Analysis for X-ray Absorption Spectroscopy Using IFEFFIT. *J. Synchrotron Rad.* **2005**, *12*, 537–541.

(46) Kresse, G.; Hafner, J. Ab Initio Molecular Dynamics for Liquid Metals. *Phys. Rev. B* **1993**, *47*, 558–561.

(47) Kresse, G.; Hafner, J. Ab Initio Molecular-dynamics Simulation of the Liquid-Metal–Amorphous-Semiconductor Transition in Germanium. *Phys. Rev. B* **1994**, *49*, 14251–14269.

(48) Kresse, G.; Furthmüller, J. Efficient Iterative Schemes for Ab Initio Total-Energy Calculations Using a Plane-Wave Basis Set. *Phys. Rev. B* **1996**, *54*, 11169–11186.

(49) Kresse, G.; Furthmüller, J. Efficiency of Ab-Initio Total Energy Calculations for Metals and Semiconductors Using a Plane-Wave Basis Set. *Comput. Mater. Sci.* **1996**, *6*, 15–50.

(50) Perdew, J. P.; Burke, K.; Ernzerhof, M. Generalized Gradient Approximation Made Simple. *Phys. Rev. Lett.* **1996**, *77*, 3865–3868.

(51) Momma, K.; Izumi, F. VESTA 3 for Three-Dimensional Visualization of Crystal, Volumetric and Morphology Data. *J. Appl. Crystallogr.* **2011**, *44*, 1272–1276.

(52) Qian, S.; Yu, H.; Yan, L.; Zhu, H.; Cheng, X.; Xie, Y.; Long, N.; Shui, M.; Shu, J. High-Rate Long-Life Pored Nanoribbon VNb_9O_{25} Built by Interconnected Ultrafine Nanoparticles as Anode for Lithium-Ion Batteries. *ACS Appl. Mater. Interfaces* **2017**, *9*, 30608–30616.

(53) See, K. A.; Lumley, M. A.; Stucky, G. D.; Grey, C. P.; Seshadri, R. Reversible Capacity of Conductive Carbon Additives at Low Potentials: Caveats for Testing Alternative Anode Materials for Li-Ion Batteries. *J. Electrochem. Soc.* **2017**, *164*, A327–A333.

(54) Angerstein-Kozlowska, H.; Klinger, J.; Conway, B. Computer Simulation of the Kinetic Behaviour of Surface Reactions Driven by a Linear Potential Sweep: Part I. Model 1-Electron Reaction with a Single Adsorbed Species. *J. Electroanal. Chem. Interfacial Electrochem.* **1977**, *75*, 45–60.

(55) Augustyn, V.; Come, J.; Lowe, M. A.; Kim, J. W.; Taberna, P.-L.; Tolbert, S. H.; Abruña, H. D.; Simon, P.; Dunn, B. High-Rate Electrochemical Energy Storage Through Li^+ Intercalation Pseudocapacitance. *Nat. Mater.* **2013**, *12*, 518–522.

(56) Augustyn, V.; Simon, P.; Dunn, B. Pseudocapacitive Oxide Materials for High-Rate Electrochemical Energy Storage. *Energy Environ. Sci.* **2014**, *7*, 1597–1614.

(57) McHenry, M. E.; Laughlin, D. E. In *Characterization of Materials*, 2nd ed.; Kaufmann, E. N., Ed.; John Wiley & Sons, Inc.: Hoboken, NJ, USA, 2012.

(58) Mott, N. F. The Effect of Electron Interaction on Variable-Range Hopping. *Phil. Mag. A* **1976**, *34*, 643–645.

Graphical TOC Entry

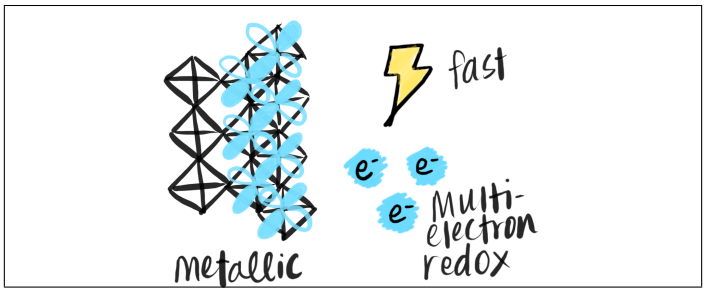

SI for Multielectron Redox and Insulator-to-metal Transition upon Lithium Insertion in the Fast-Charging, Wadsley-Roth Phase PNb_9O_{25}

Molleigh B. Preefer,[†,‡] Muna Saber,[¶] Qiulong Wei,[§] Nicholas H. Bashian,[‖] Joshua D. Bocarsly,[‡,⊥] William Zhang,[†] Glenn Lee,[§] JoAnna Milam-Guerrero,[‖] Erica S. Howard,[‖] Rebecca C. Vincent,[‡,⊥] Brent C. Melot,[‖] Anton Van der Ven,[*,⊥] Ram Seshadri,[*,‡,⊥,†] and Bruce S. Dunn[*,§]

†*Department of Chemistry and Biochemistry, University of California Santa Barbara, California 93106, United States*

‡*Materials Research Laboratory, University of California Santa Barbara, California 93106, United States*

¶*Department of Chemical Engineering, University of California Santa Barbara, California 93106, United States*

§*Department of Materials Science and Engineering, University of California Los Angeles, California 90095, United States*

‖*Department of Chemistry, University of Southern California Los Angeles, California 90089, United States*

⊥*Materials Department, University of California Santa Barbara, California 93106, United States*

E-mail: avdv@ucsb.edu; seshadri@mrl.ucsb.edu; bdunn@ucla.edu

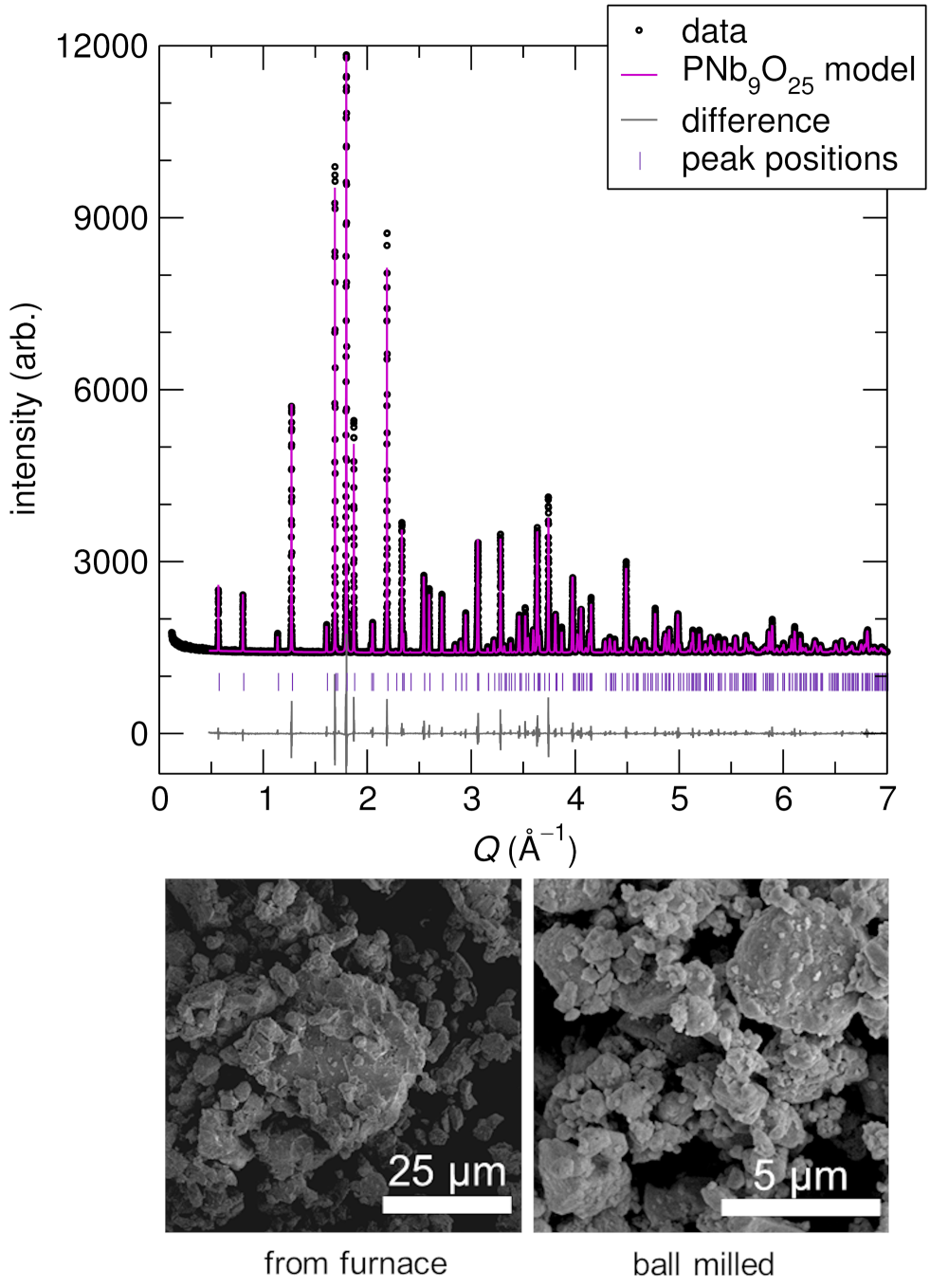

Figure S1: PNb_9O_{25} was synthesized by solid state methods as described in the main text. Rietveld refinement of high-resolution synchrotron powder XRD from beamline 11-BM at the Advanced Photon Source revealed the sample to be single phase, and the Bragg reflections are shown below for reference. $R_{wp} = 15.1$, $R_{exp} = 10.3$, and GOF = R_{wp}/R_{exp} =1.46, with the cell parameters a = 15.61810(4) Å and c = 3.82869(1) Å. Additionally, the SEM images from the as-prepared sample and the ball-milled sample show that all of the electrochemistry and characterization has been done using micron-sized particles. Primary particles are on the order of 1 μm. Images were collected using a FEI Nova Nano 650 FEG SEM on uncoated pristine powder.

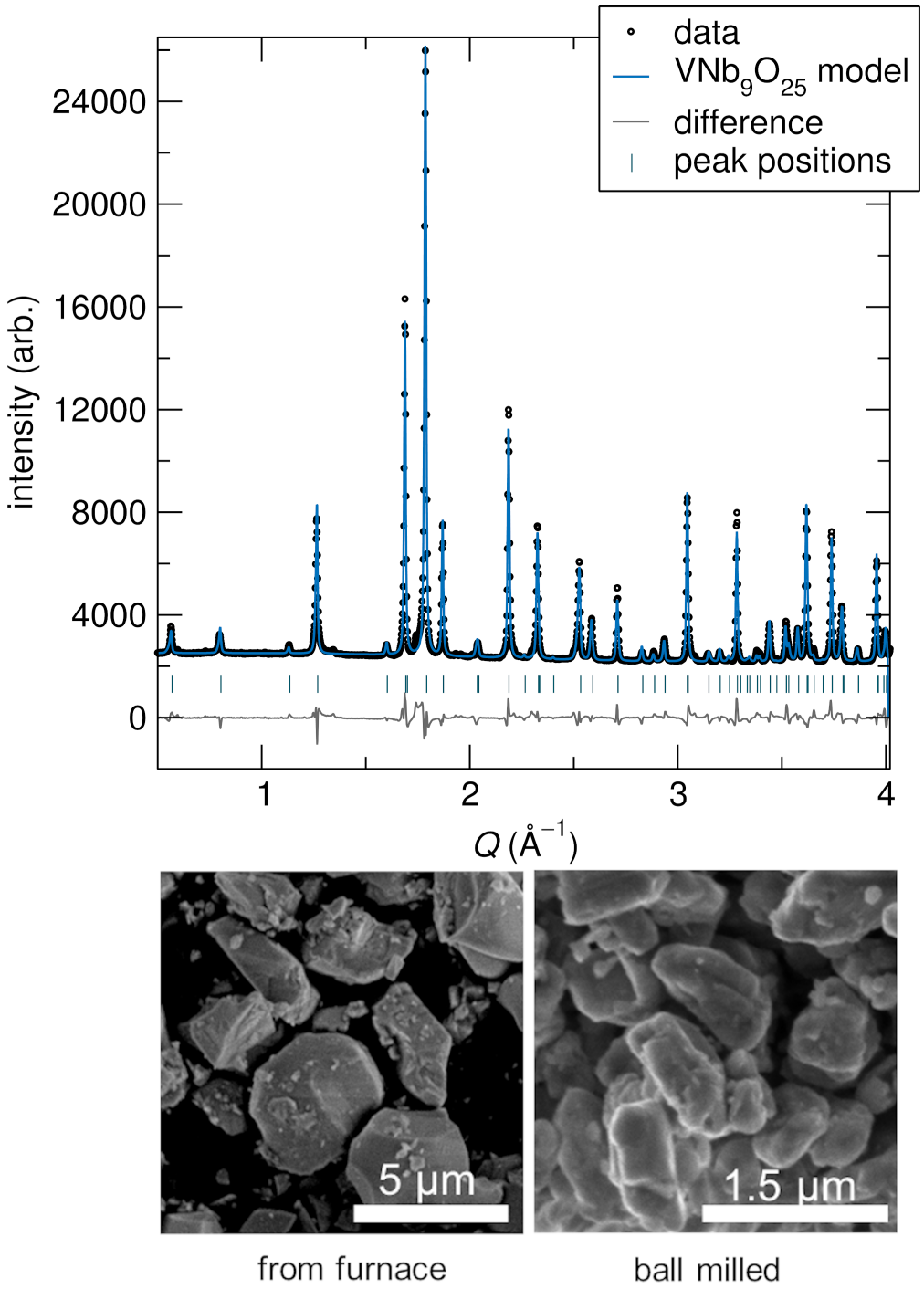

Figure S2: PNb_9O_{25} was synthesized by solid state methods as described in the main text. Synchrotron powder XRD from beamline 17-BM at the Advanced Photon Source and subsequent Rietveld refinement confirm the successful synthesis of VNb_9O_{25}. The obtained lattice parameters are $a = 15.7101(7)$ and $c = 3.8284(2)$. $R_{wp} = 4.00$, $R_{exp} = 1.88$, and GOF = R_{wp}/R_{exp} =2.13. The sample was subsequently ball-milled, and SEM reveals the particle size of the primary particles is on the order of 1 μm. Images were collected using a FEI Nova Nano 650 FEG SEM on uncoated pristine powder.

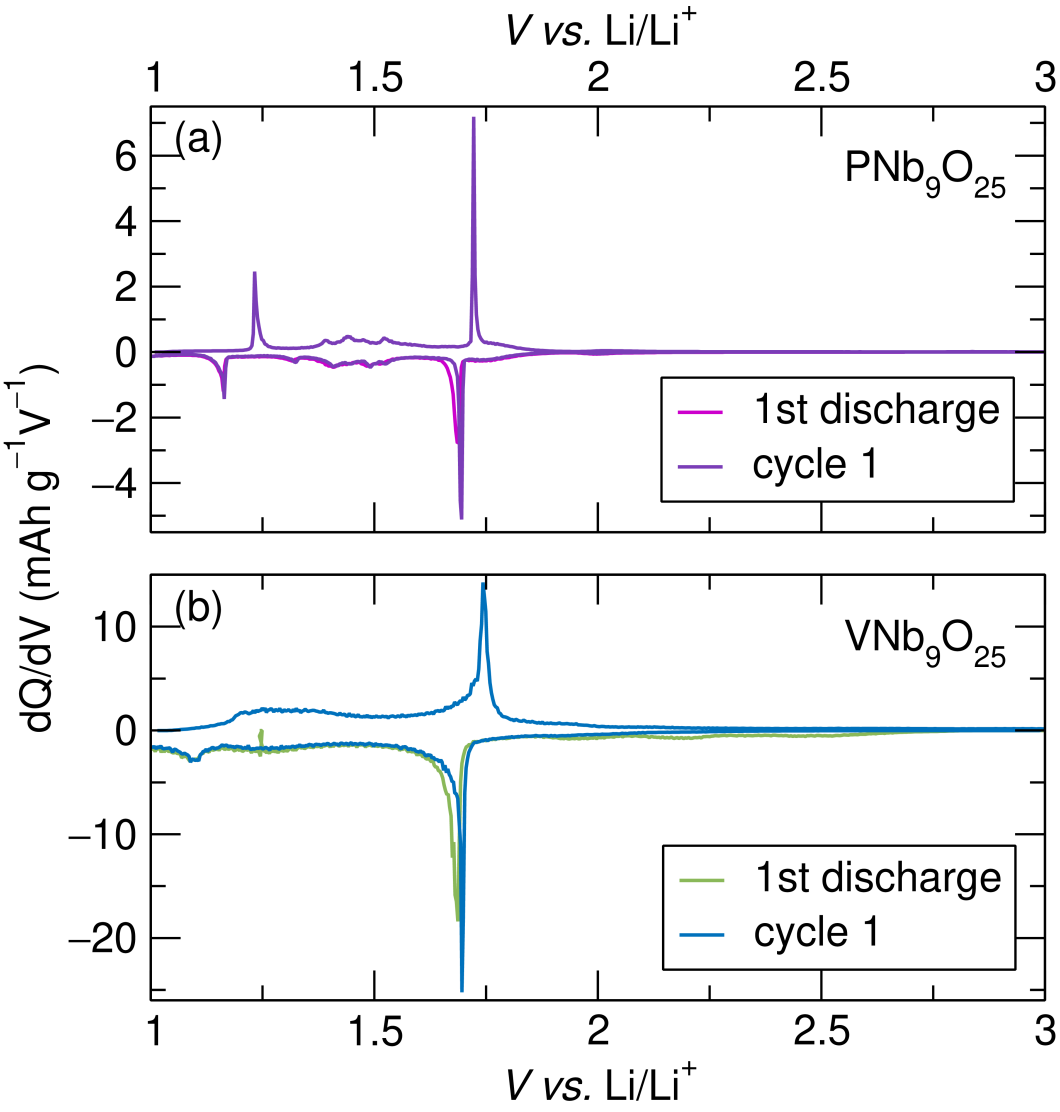

Figure S3: Derivative curves calculated from the first discharge, first charge, and second discharge of the C/20 galvanostatic cycling traces from PNb_9O_{25} (a) and VNb_9O_{25} (b).

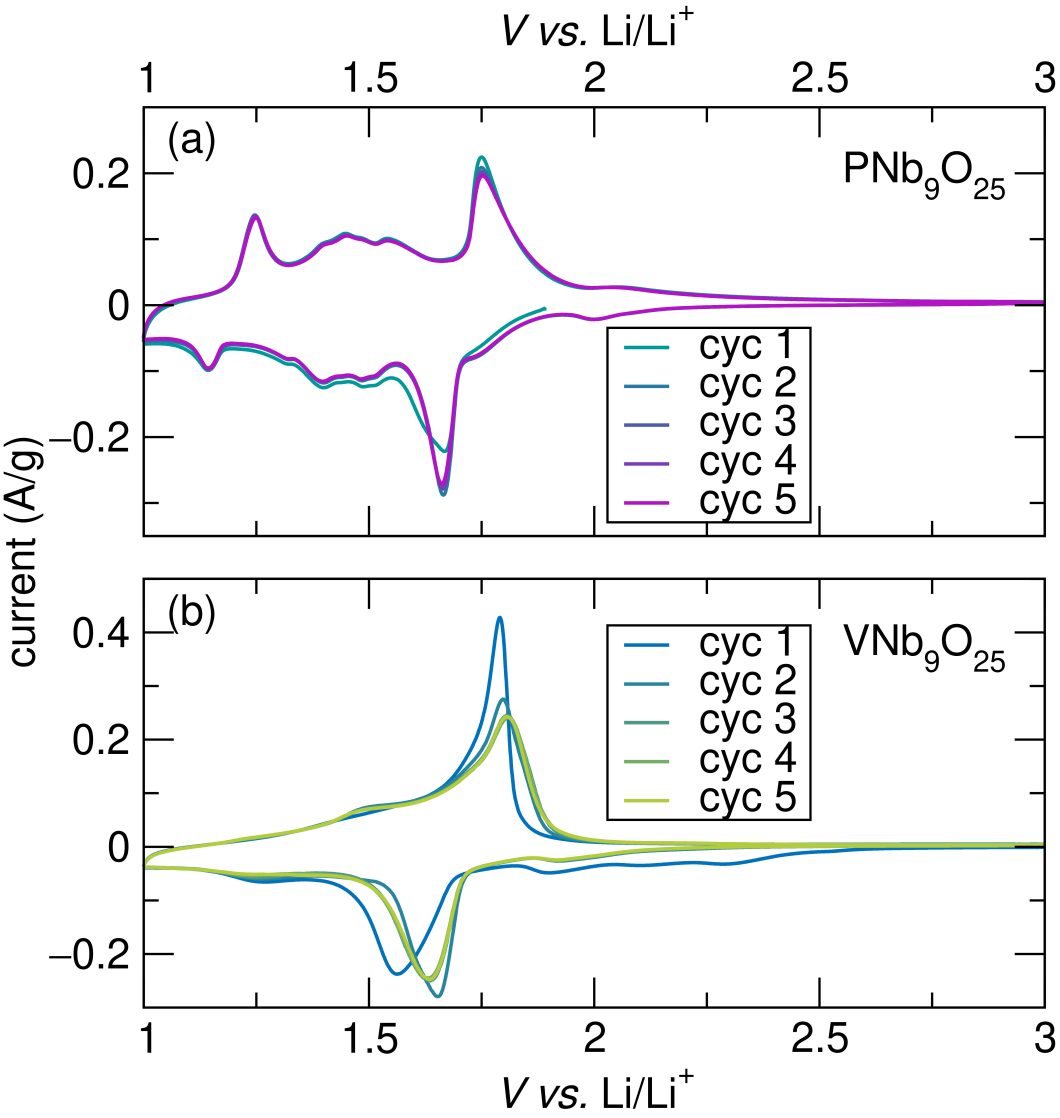

Figure S4: Expanded cyclic voltammagrams at 0.1 mV/s for PNb_9O_{25} (a) and VNb_9O_{25} (b).

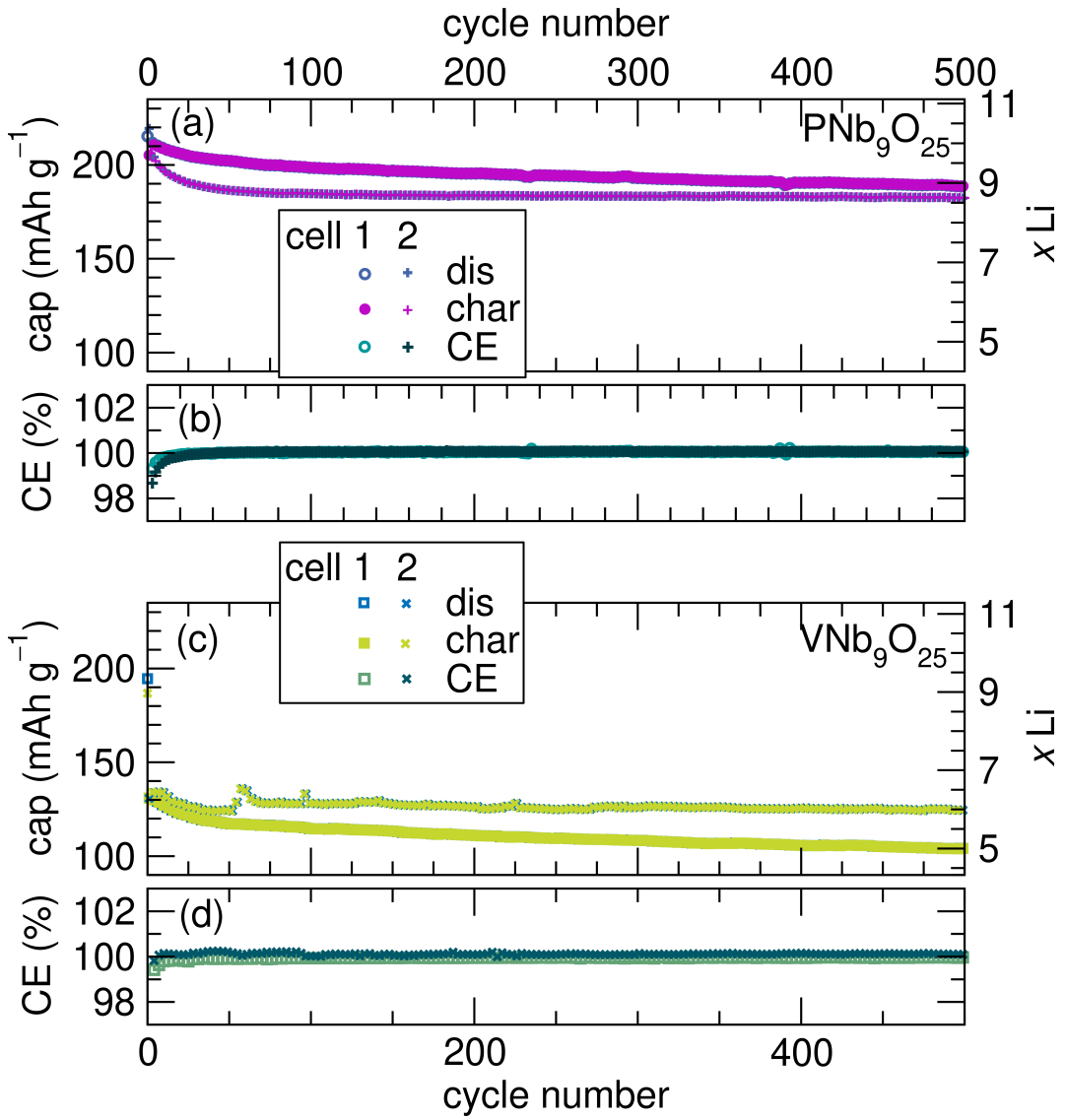

Figure S5: Replicate cells for PNb_9O_{25} and VNb_9O_{25} show similar behavior and capacities at 2C over 500 cycles. (a) Capacity as a function of cycle number for PNb_9O_{25} in two distinct coin cells prepared according to the description in the main text and (b) the corresponding Coulombic efficiencies (CE) as a percentage. (c) Capacity as a function of cycle number for VNb_9O_{25} in two distinct coin cells prepared according to the description in the main text and (d) the corresponding Coulombic efficiencies (CE) as a percentage. After the first 5 cycles across all cells and materials, the discharge and charge capacities within each cycle are roughly even.

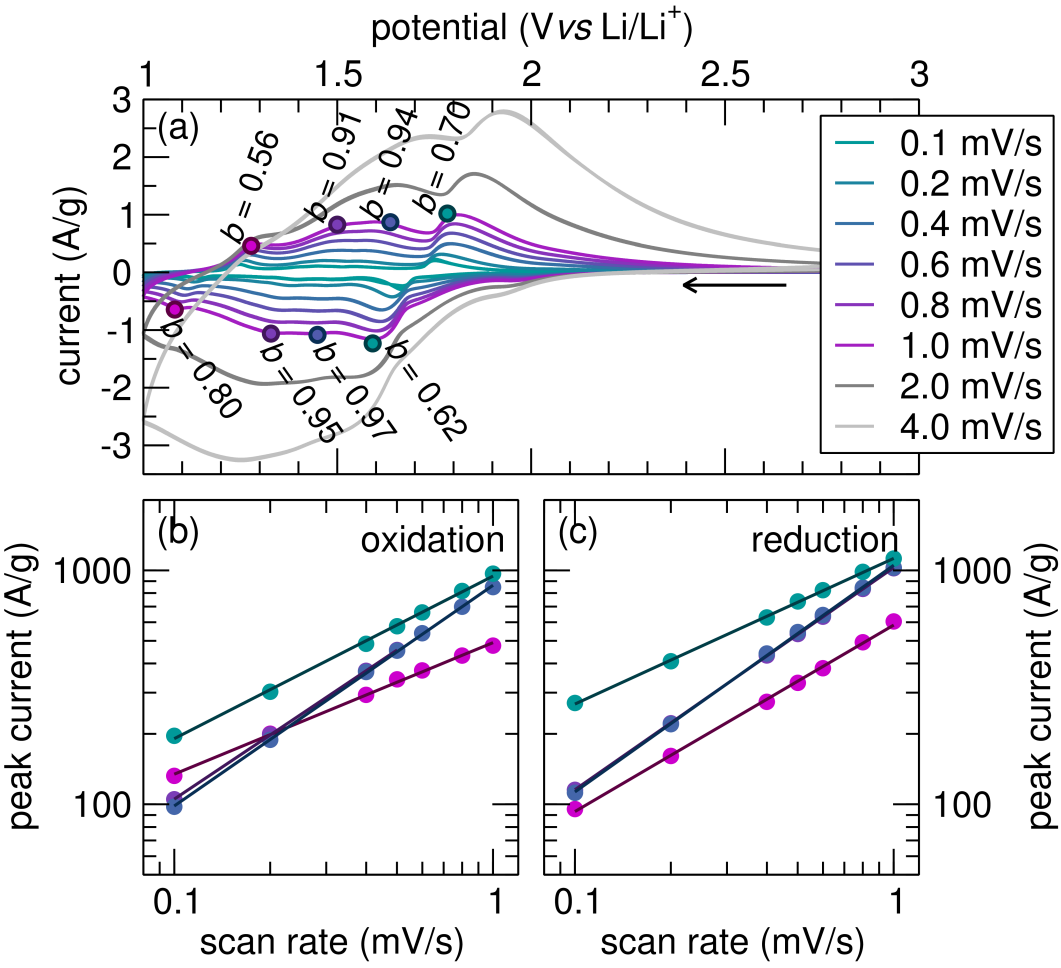

Figure S6: Cyclic voltammetry of PNb_9O_{25} at varying sweep rates and the b-values overlaid at the corresponding redox peaks (a). Power law fits for each oxidation peak as a result of relating the scan rate and current (b). Power law fits for each oxidation peak as a result of relating the scan rate and current (c).

Table 1: The corresponding equations and coefficient of determination that fit the relationship between current and sweep rate for PNb_9O_{25}.

	avg.	***b*-value**	**power law fit**	$\mathbf{R^2}$
red	1.11 V	0.80	$y = 583.9x^{0.7969}$	0.998
	1.37 V	0.95	$y = 1028.6x^{0.9499}$	0.999
	1.46 V	0.97	$y = 1051.2x^{0.9686}$	0.999
	1.62 V	0.62	$y = 1126.1x^{0.6225}$	0.999
ox	1.28 V	0.56	$y = 491.48x^{0.5628}$	0.998
	1.49 V	0.91	$y = 857.17x^{0.9109}$	0.999
	1.57 V	0.94	$y = 864.07x^{0.9438}$	0.999
	1.79 V	0.70	$y = 945.44x^{0.6953}$	0.998

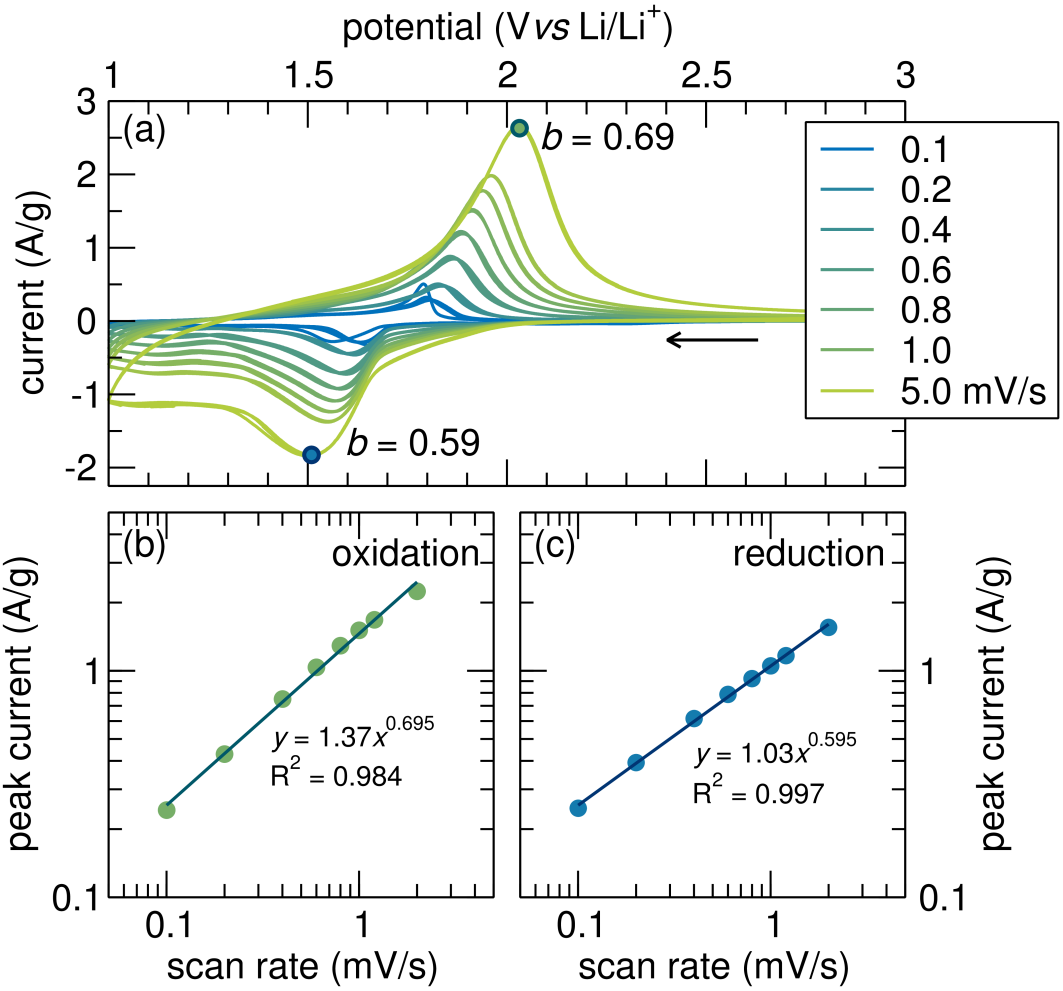

Figure S7: Cyclic voltammetry of VNb_9O_{25} at varying sweep rates and the b-values overlaid at the corresponding redox peaks (a). Power law fits for each oxidation peak as a result of relating the scan rate and current (b). Power law fits for each oxidation peak as a result of relating the scan rate and current (c).

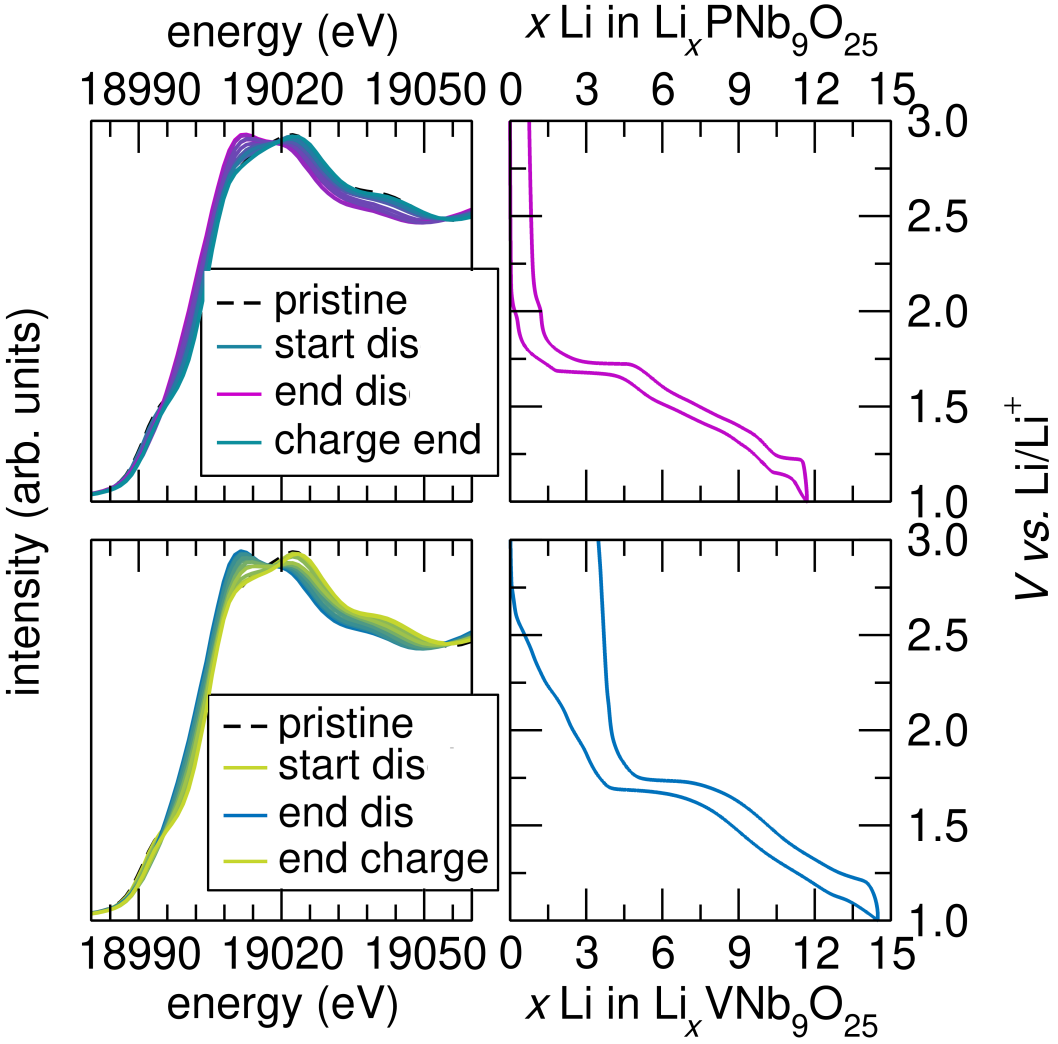

Figure S8: *Operando* XANES data for PNb_9O_{25} and VNb_9O_{25} with the corresponding galvanostatic cycling for the first cycle during which the data was collected at a rate of C/10. The electrochemical data observed in the AMPIX cells reflect the same trace observed from data collected in coin cells.

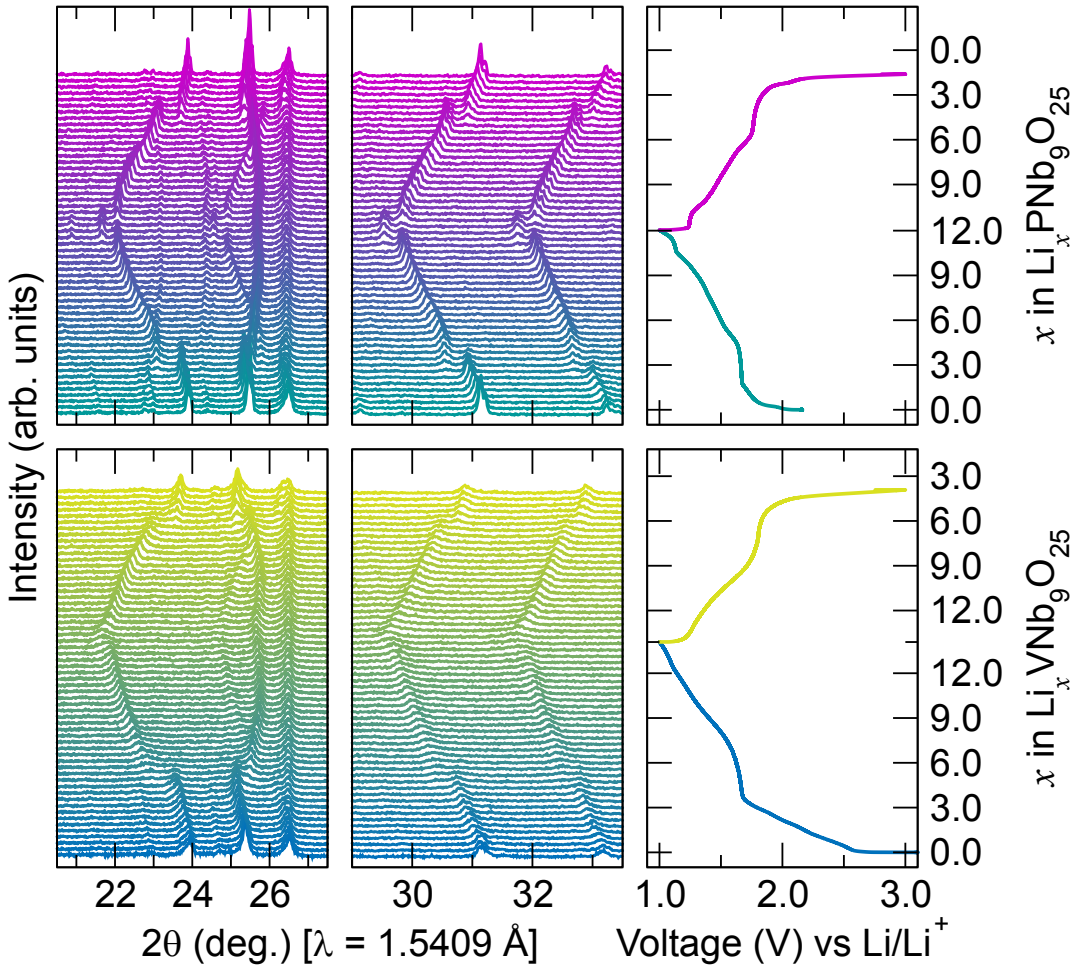

Figure S9: *Operando* XRD for PNb_9O_{25} (top) and VNb_9O_{25} (bottom) during the first galvanostatic cycle at a rate of C/10 shows the structural transformations as the materials are cycled. Both compounds have an initial unit cell expansion in common, corresponding to the discharge plateau at 1.7 V. After they get in formation, they both show reversible cycling, recovering the initial powder pattern prior to cycling. *Operando* XRD measurements were performed using a Bruker D8 diffractometer with a Cu K_α source (λ_1 = 1.5406 Å, λ_2 = 1.5444 Å), equipped with a Lynxeye XE-T detector. A modified Swagelok cell, with Be window serving as a current collector, allowed for diffraction patterns to be collected during electrochemical cycling. XRD scans were collected in a Bragg-Brentano geometry over a range of 20°, to 50°, 2θ with a total scan time of 20 minutes.

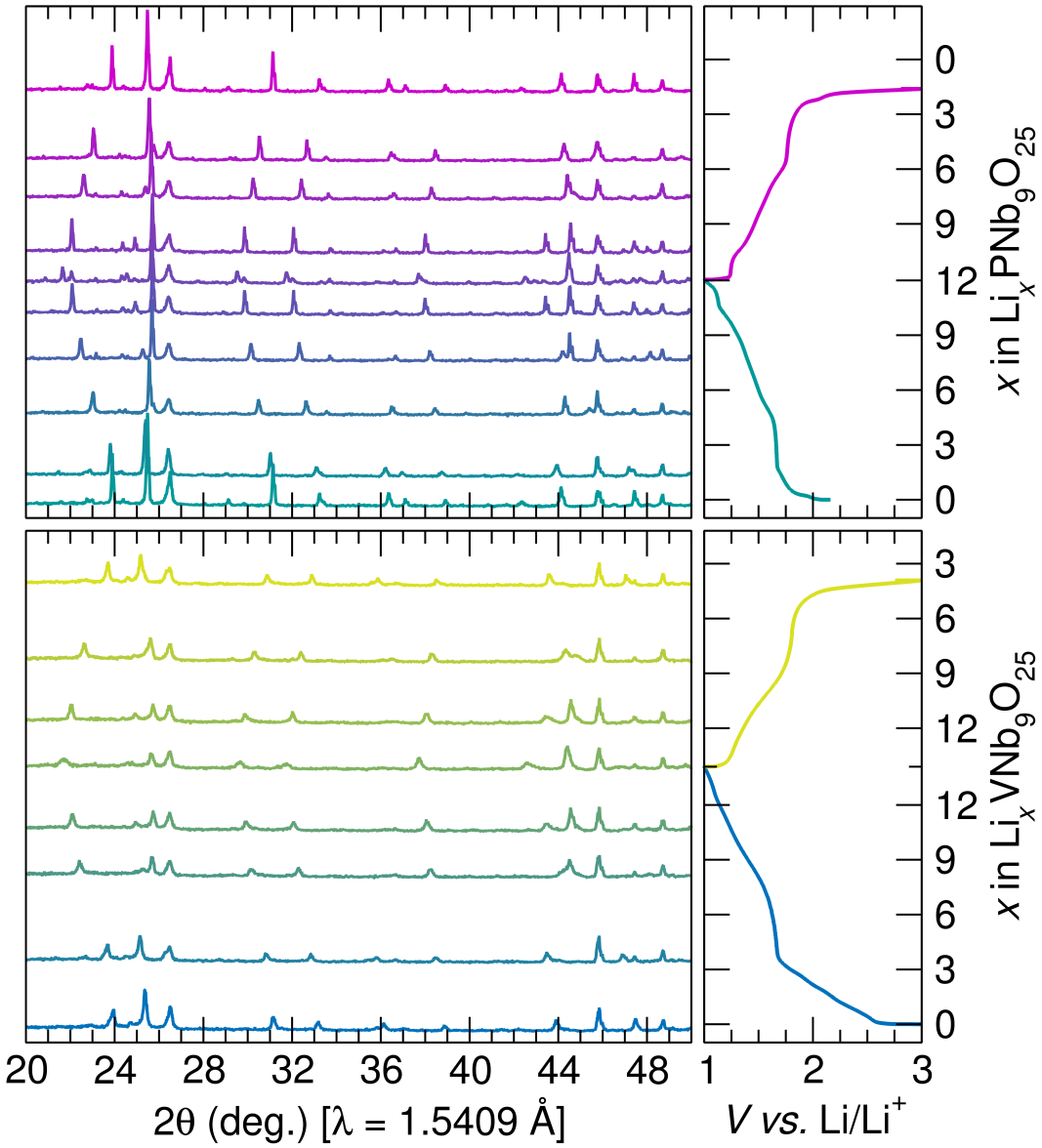

Figure S10: Select patterns from the *operando* XRD for PNb_9O_{25} (top) and VNb_9O_{25} (bottom) during the first galvanostatic cycle at a rate of C/10.

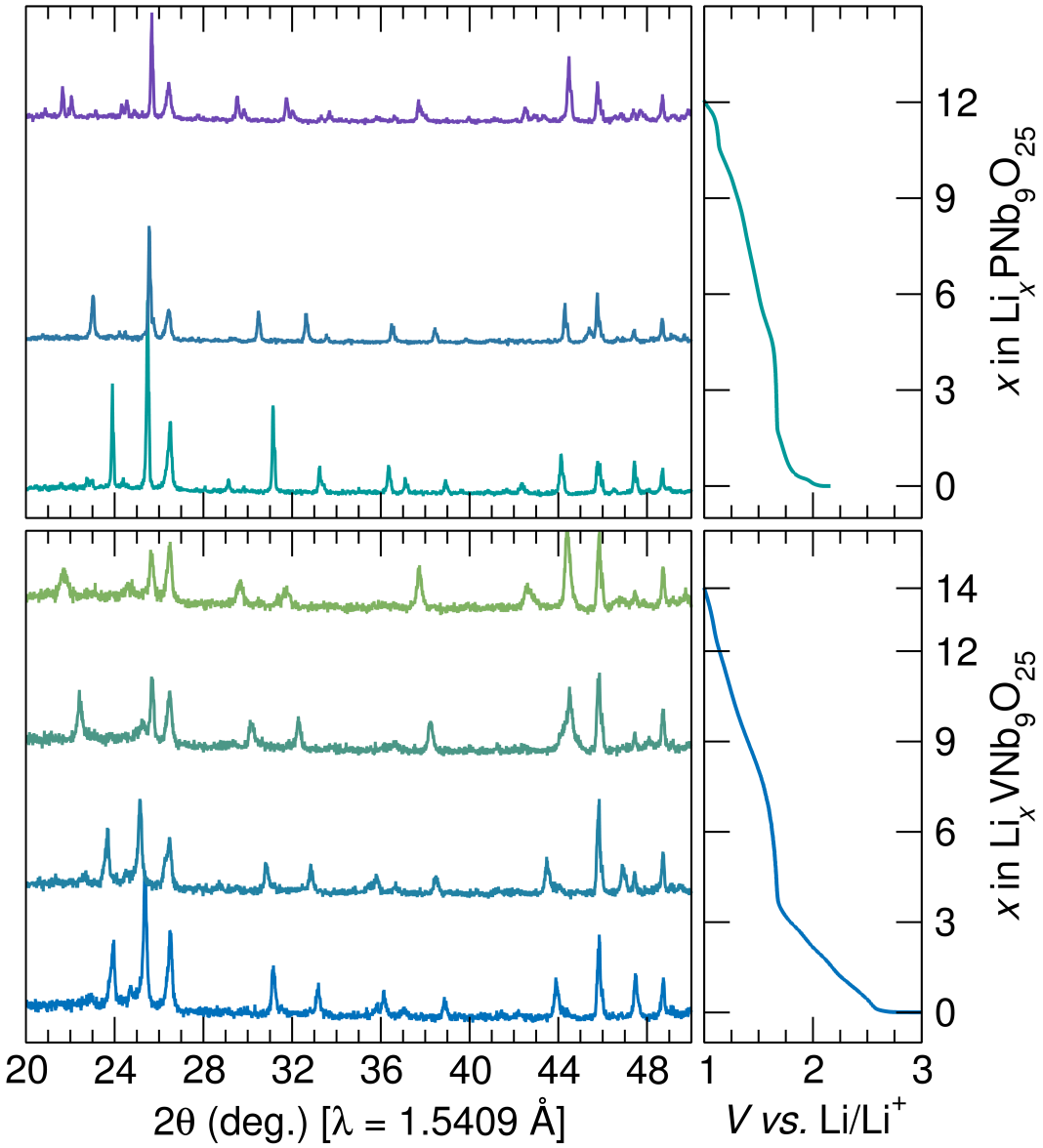

Figure S11: Select patterns from the *operando* XRD for PNb_9O_{25} (top) and VNb_9O_{25} (bottom) during the first discharge at a rate of C/10.

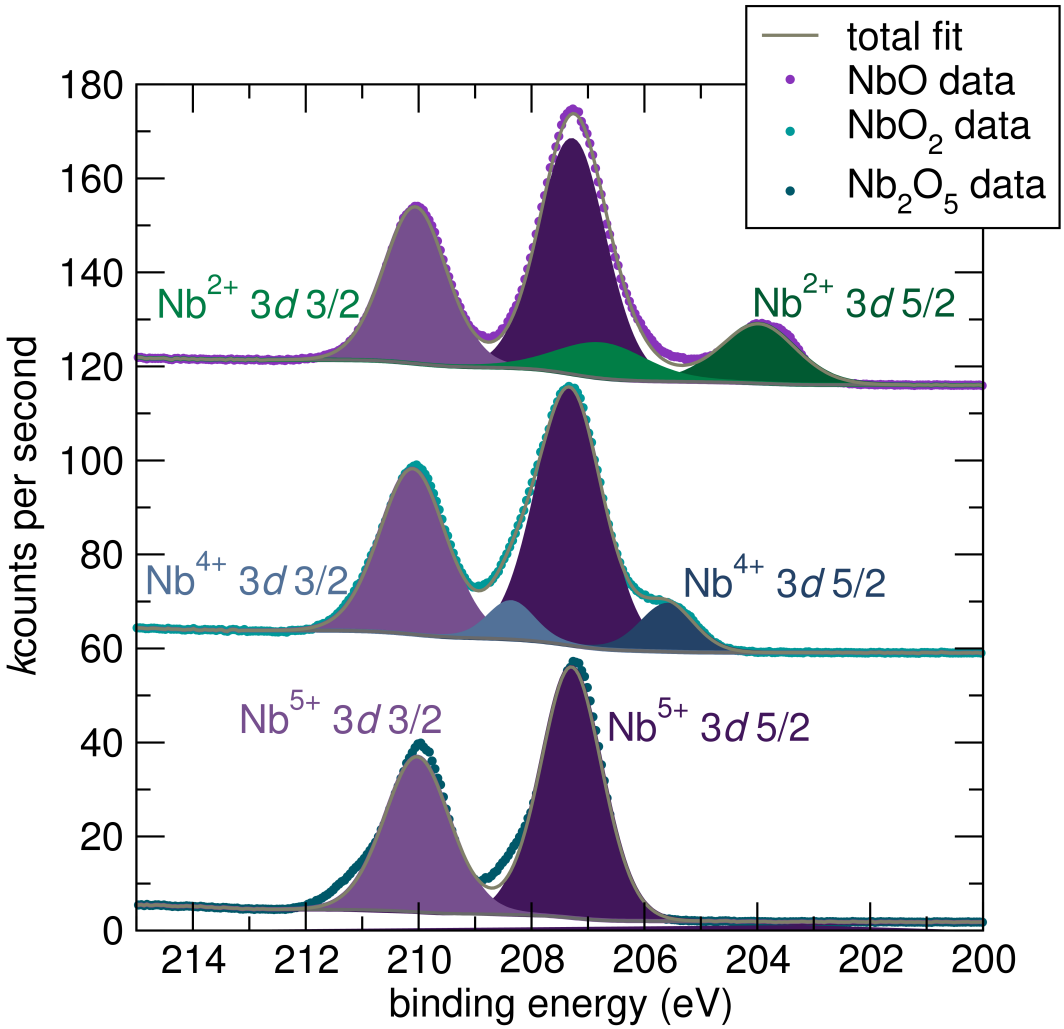

Figure S12: Standards sourced from Sigma Aldrich (Nb_2O_5, NbO_2) and prepared via arc melting Nb and Nb_2O_5 (NbO). They were measured using the same spectrometer and settings used for the Nb high resolution regions in the samples of interest. The oxidation states are in agreement with other literature values. There is significant surface oxidation in NbO_2 and NbO, but the reduced states are still prominent for fitting purposes. The shifts observed for the respective oxidation states were used to assign oxidation states in PNb_9O_{25} and VNb_9O_{25}.

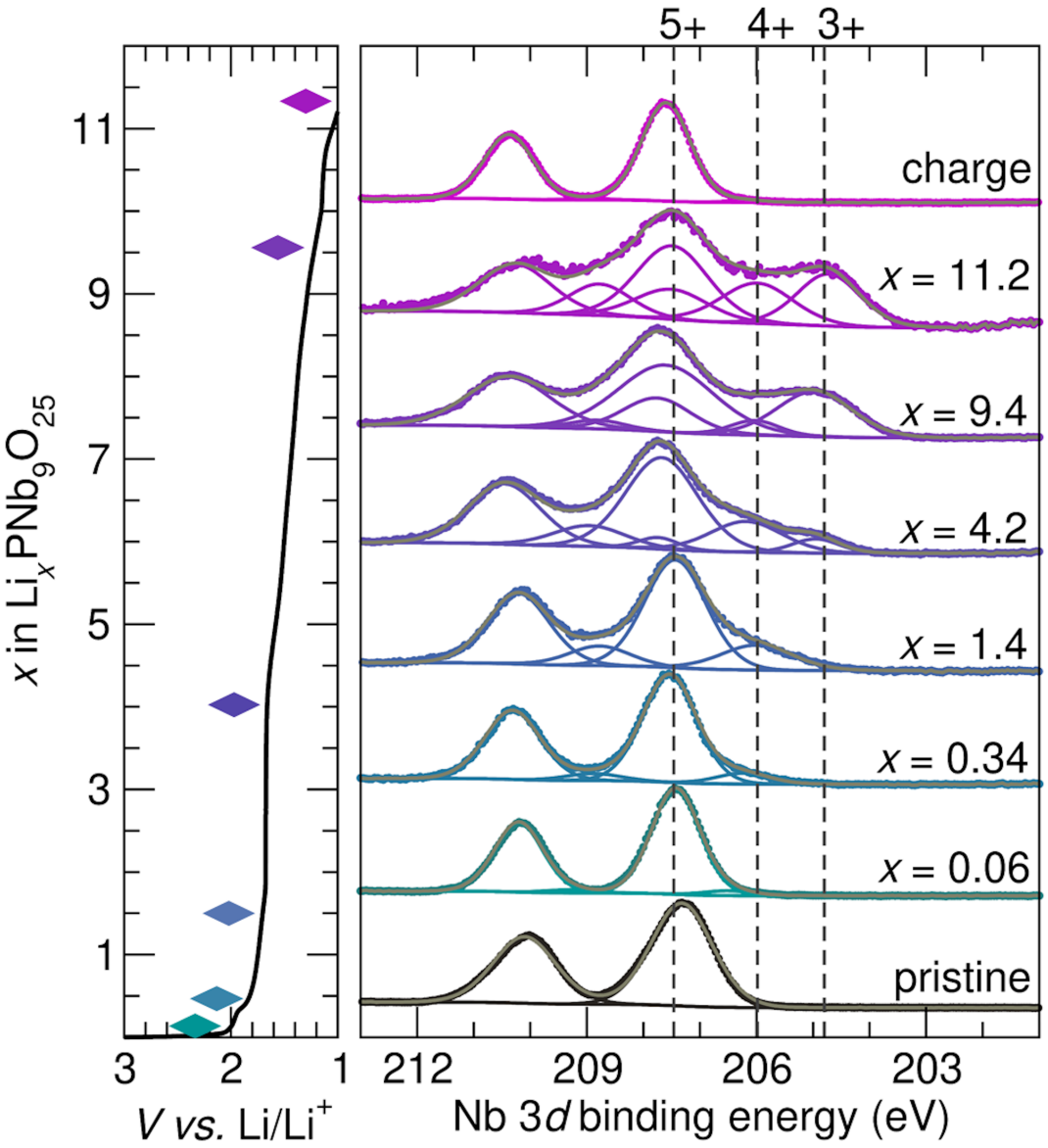

Figure S13: Expanded view of the Nb states for PNb_9O_{25} with expected shifts for Nb^{5+}, Nb^{4+}, and Nb^{3+}.

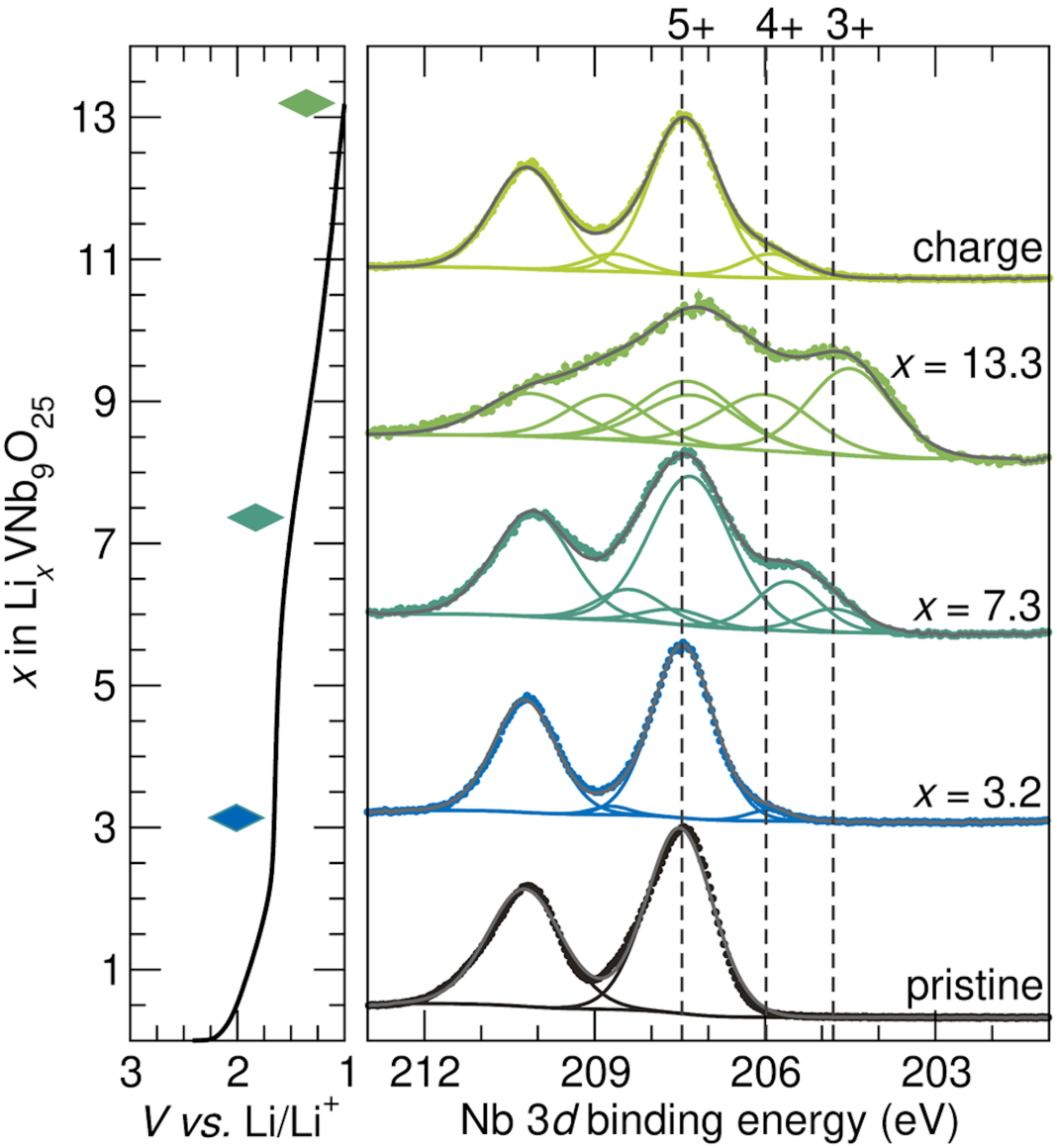

Figure S14: Expanded view of the Nb states for VNb_9O_{25} with expected shifts for Nb^{5+}, Nb^{4+}, and Nb^{3+}.

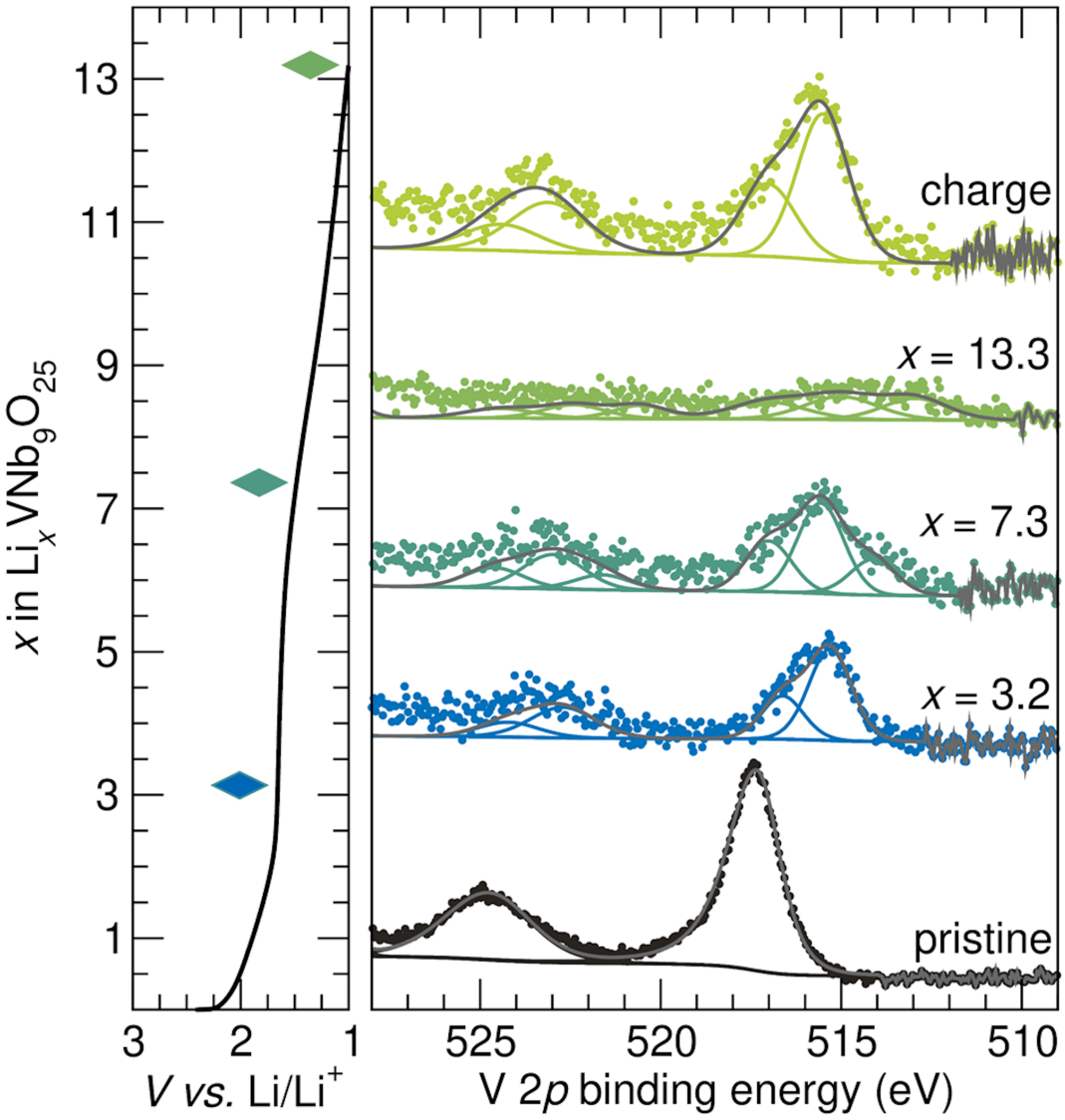

Figure S15: Expanded view of the V states for VNb_9O_{25}. For completeness, the spectra were fit according to expected peak positions and constraints for V^{5+}, V^{4+}, and V^{3+}, however low signal-to-noise prevents quantitative analysis. Qualitative assessments can be made, though. The smearing of intensity especially at highest lithiation suggests the emergence of V^{3+}, and the peaks become sharper again (intensity in a narrower spectral region), which suggests reoxidation to a combination of V^{5+} and V^{4+}.

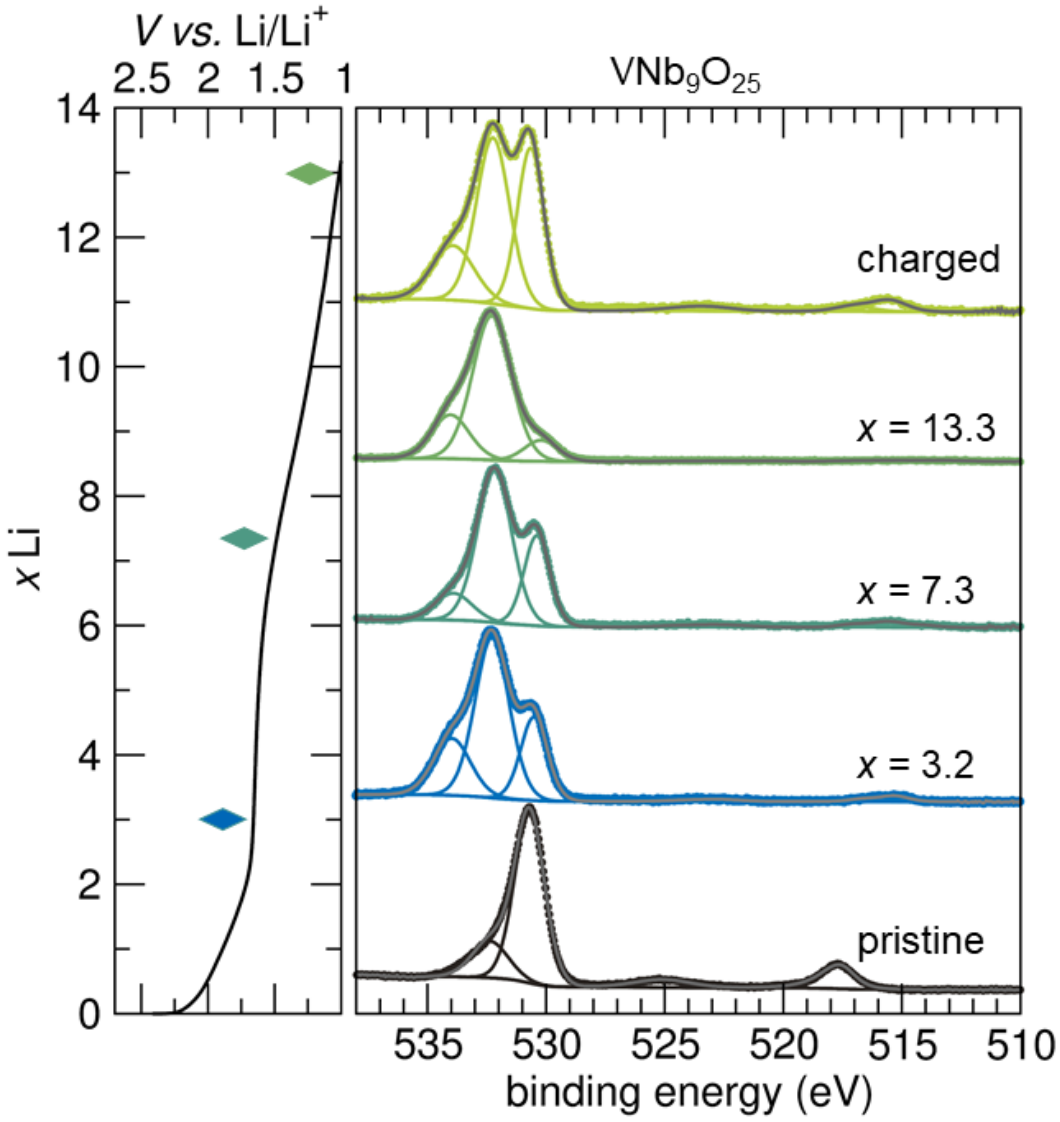

Figure S16: XPS showing the full spectral region for O $1s$ and V $2p$ at the specified states of charge mapped onto the discharge curve (left), which, for accuracy, have been fitted together. Since vanadium is not very abundant in VNb_9O_{25}, the signal for the V 2p region is much weaker than the O $1s$ region. The O $1s$ region illustrates a convolution of the M-O reduction between the V-O sites and the Nb-O sites, heavily weighted toward the Nb octahedra. The addition of higher BE peaks as the material is reduced reflects reduction of the transition metal.

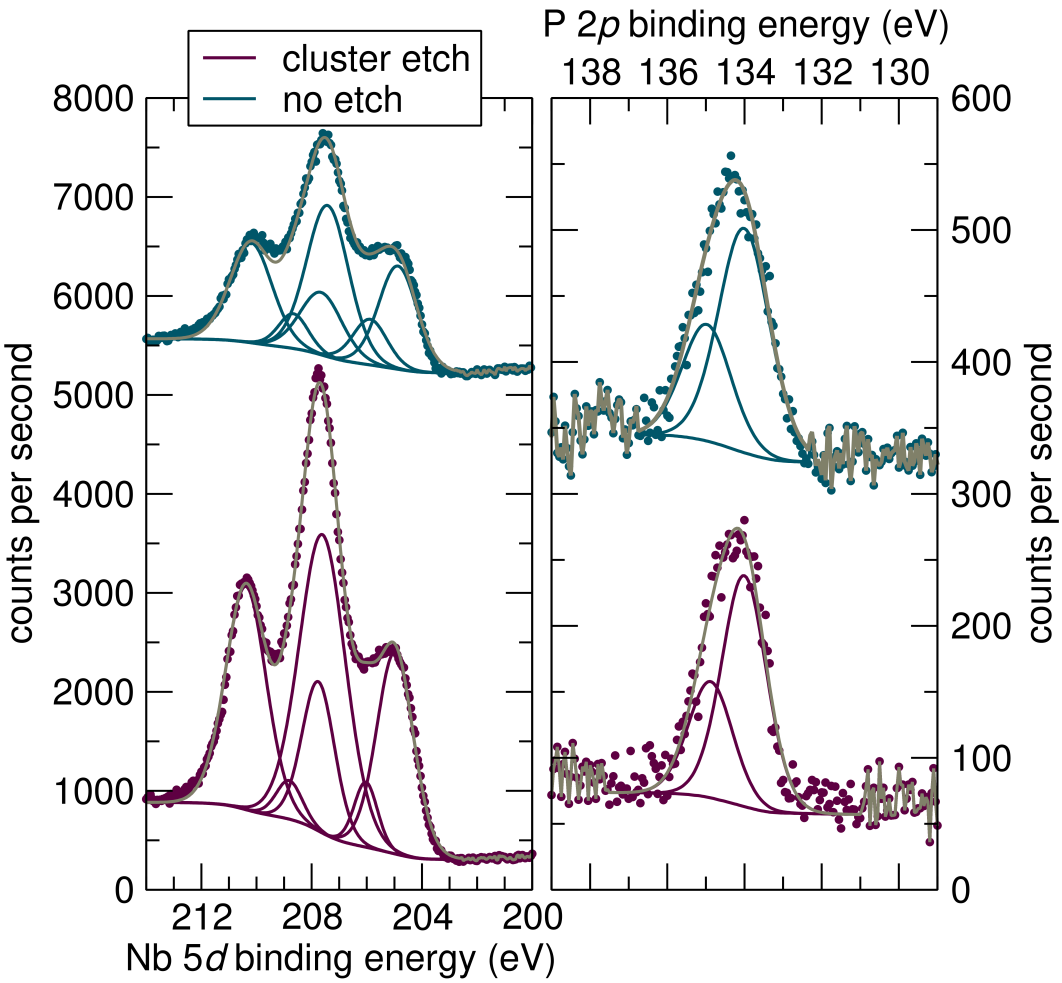

Figure S17: High resolution comparisons between the same PNb_9O_{25} sample (x = 9.4 Li) both Ar etched (bottom) and not etched (top). The left shows the Nb 3d region for both, not scaled to compare the difference in intensity. Etching removes much of the SEI layer, which reveals higher Nb intensity, which is then closer to the surface of the sample. Despite the difference in intensity, the fits are very similar in both position and areas. The right shows the P 2p region, where Ar etching has the opposite effect – since P is present in the SEI layer, intensity is slightly decreased after etching. However, there is no discernible difference in binding energies or number of states present in the etched and non-etched sample. This suggests etching is not necessary for getting a spectrum representative of the active material at different states of charge as prepared.

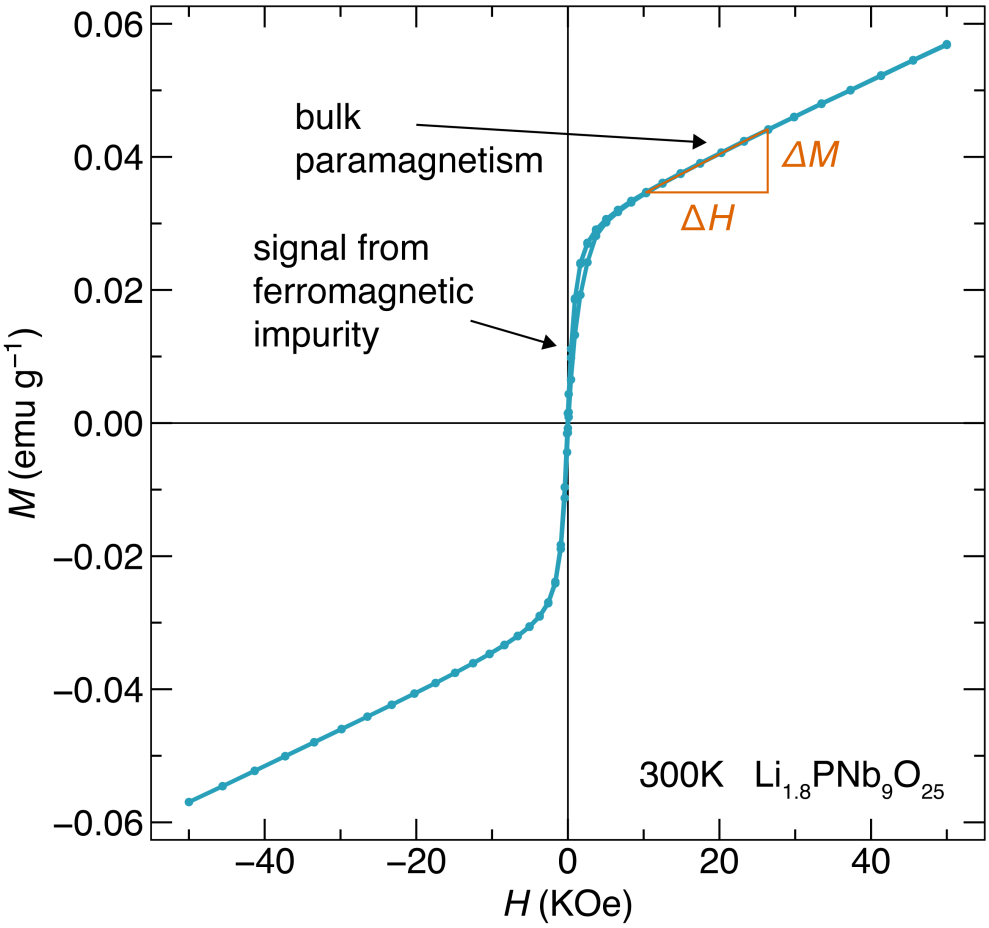

Figure S18: Room-temperature magnetization *vs.* field measurements for *ex situ* samples of $Li_xPNb_9O_{25}$ showed the presence of very small quantities of ferromagnetic impurities, which were traced back to the use of steel ball mill during electrode fabrication. As a result, the samples showed a $M(H)$ curve as displayed here for $Li_{1.8}PNb_9O_{25}$. At low fields, a ferromagnetic impurity signal is seen. Fortunately, this signal saturates at moderate fields, and the expected linear $M(H)$ of the bulk paramagnetic sample can be clearly observed at higher fields. The observed magnitude of the ferromagnetic impurity signal is consistent with the presence of just 0.01 wt-% iron metal ($M_{\text{sat}} = 217\,\text{emu}\,\text{g}^{-1}$). In order to correctly calculate the magnetic susceptibility of the $Li_xPNb_9O_{25}$ phase, a differential calculation is performed as illustrated on the graphic. For each temperature, magnetization is measured at two different fields (5 kOe and 10 kOe for $Li_{1.8}PNb_9O_{25}$ and $Li_{11.2}PNb_9O_{25}$ and 20 kOe and 30 kOe for $Li_8PNb_9O_{25}$) and the susceptibility χ is calculated as $\Delta M/\Delta H$.

Electrochemical impedance spectroscopy

$Li_xPNb_9O_{25}$ at discrete lithiated states was prepared in 1.5 inch diameter Swagelok cells to accommodate approximately 100 mg of pure PNb_9O_{25} powder in a thin layer without the addition of binder or carbon. The active material was cycled against polished Li metal using 1 M $LiPF_6$ in EC/DMC 50/50 *v/v* (Sigma Aldrich). The cells were discharged at a C/60 rate to the chosen potentials. The active material was extracted from the cells in an Ar-filled glovebox and ground with an agate mortar and pestle. In order to probe the intrinsic conductivity, the samples were washed three times with dimethyl carbonate in order to remove $LiPF_6$ from the electrolyte, centrifuged, and dried under vacuum. Approximately 60 mg of powder was pressed into a blocking electrode cell, using stainless steel plungers and a Delrin body (electrically insulating). A full description of the cell and setup has been previously reported in Preefer, M.B.; Grebenkemper, J.H.; Schroeder, F.; Bocarsly, J.D.; Pilar, K.; Cooley, J.A.; Zhang, W.; Hu, J.; Misra, S.; Seeler, F.; Schierle-Arndt, K.; Seshadri, R. Rapid and Tunable Assisted-Microwave Preparation of Glass and Glass-Ceramic Thiophosphate "$Li_7P_3S_{11}$" Li-Ion Conductors. *ACS Appl. Mater. Interfaces* **2018,** *11*, 42280–42287. The end caps are greased in order to maintain an air-free environment within the cell. The material was cold pressed to 10 MPa, then transferred to an environmental chamber and continuously pressed to approximately 100 MPa using a vise and a load cell for monitoring the force. Before measurements were started, the material densifies under these conditions for 15 hours. The conditions for the electrochemical impedance spectroscopy measurements are as follows: 1 MHz to 100 mHz at an amplitude of 25 mV to 100 mV, depending on the signal from each sample, averaged twice per measurement, with 10 points per decade. Temperature was swept from 258.15 K to 318.15 K, and the samples were allowed to equilibrate for 45 minutes. in between each temperature point.

The absence of a Warburg tail in the data points to the conductivity measurements being overwhelmed by electronic conductivity, and only one semicircle could be fit in a simple equivalence circuit of a resistor and capacitor in parallel. Therefore, the total resistance

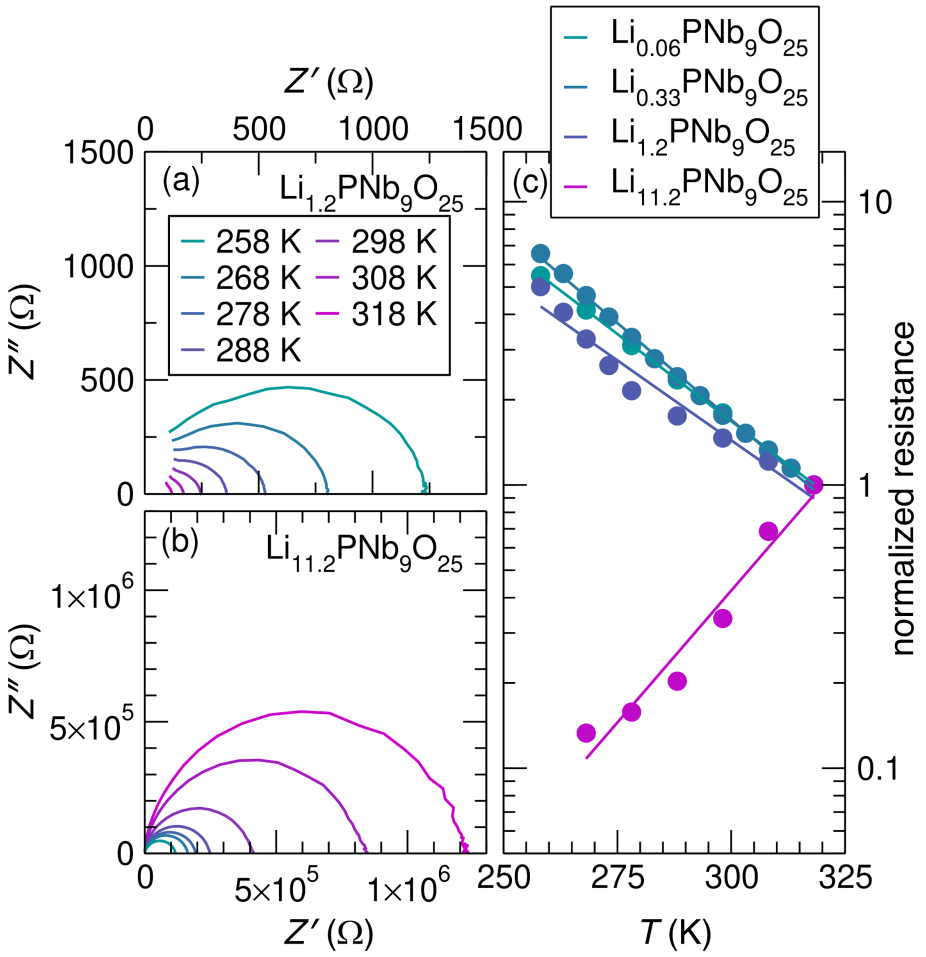

Figure S19: (a) Nyquist plot of $Li_{1.2}PNb_9O_{25}$ washed free of $LiPF_6$ from 256 K to 318 K such that only the intrinsic conductivity is measured. Resistance decreases with increasing temperature in low lithiated states. (b) Nyquist plot of $Li_{11.2}PNb_9O_{25}$ washed free of $LiPF_6$ from 256 K to 318 K. Resistance increases with increasing temperature in high lithiated states. (c) Resistance normalized to the highest temperature value for discrete states of lithiation, suggesting that PNb_9O_{25} undergoes an insulator-to-metal transition at higher states of lithiation.

found by fitting the circuit was used as an approximation for electronic conductivity. The resistance values were normalized to the resistance at the highest temperature measured to remove the influence of sintering and poorly conducting grain boundaries on the trends observed as lithium is inserted. At higher states of lithiation it is particularly challenging to densify the pellets sufficiently to ascertain the absolute value of the resistance. This is reflected in the Nyquist plots presented in which the recorded absolute resistance for the

highest lithiated state reaches the order of MΩs. Additionally, some deviation from linearity can be attributed to small deviations in the thickness of the materials as they are heated and cooled. While there is constant pressure applied, the natural expansion and contraction of the sample slightly changes the force applied by as much as 0.5 kN as monitored by a load cell. These deviations are especially pronounced in the highly lithiated sample due to the densification challenges previously mentioned. However, the trends observed by comparing the slopes of the normalized resistance as a function of temperature on a semi-log scale are indicative of how the electronic conductivity changes throughout progressive lithiation. The reversal in slope from lightly lithiated samples to highly lithiated samples suggests that $Li_xPNb_9O_{25}$ changes electronically from insulating to metallic behavior.